

Coherent Beam Combining for High Power Laser Applications

A THESIS
SUBMITTED TO THE FACULTY OF THE GRADUATE SCHOOL
OF THE UNIVERSITY OF MINNESOTA
BY

Mercedeh Khajavikhan

IN PARTIAL FULFILLMENT OF THE REQUIREMENTS
FOR THE DEGREE OF
Doctor Of Philosophy

September, 2009

© Mercedeh Khajavikhan 2009
ALL RIGHTS RESERVED

Acknowledgements

I am deeply indebted to my advisor, Professor James Leger, for his constant support. He has my outmost respect not only for his scientific insight, but also for his humanity and kindness. I was honored to have the opportunity to work with him.

I would also like to thank the members of my committee who managed to attend my final oral exam despite the short notice: Anand Gopinath, Joey Talghader, Sang-Hyun Oh, and Paul Crowell. Their advice and patience is appreciated. I would also like to thank Roger Rusack for being a member of my preliminary oral exam committee.

I would like to thank my friends and group-mates at optics group in UMN, Bing Hao, Wei Zhou, Brad Tiffany, Robert Mark, Alanna Hoyer, Chenhao Wan, Kirstin John, Jordan Burch, Hung-Sheng Chiang, Di lin, and Amy Fritz. I also like to thank Mark Fisher, Kevin Roberts, Maryam Jalali and Dave Hultman for helping me around the NFC and machine shop. Many thanks should go to the ECE administrative crew. They always find a creative way to help you.

I would also like to thank my good friends in Minnesota: Alireza, Mona, Ratnanjali, Sarah, Shahrouz, Sara, Sharareh, Baktash, Setareh, Haleh, Maryam, Yasaman, Iman, AmirHossin, Neeta, Stephanie, Sepehr and many others. These amazing people made the living in Minnesota both fine and fun.

I am also indebted to all my friends and teachers. I learned many things through discussions with my best friends : Leila, Maryam, Mahnaz, Shahrzad, Masoomeh, Mehrnaz, and Vahideh.

I have been influenced by many people in my life. Among them my father stands as the most prominent one. His enthusiasm for science and unbiased knowledge left a deep trace in my life. I am thankful to him for his encouragement and his confidence on me. I am sure he would have been the proudest and the happiest to see this dissertation. I cannot find proper words to thank my mother and the rest of my family and relatives : Azadeh, Javaher, Azarakhsh, Shideh, Aria, Azin, Akbar, Minoo, Tahereh, Ghahar, Hamid, Babak, Yaser, Siroos, Arman, Arvin, Artina, and Panetha for their continuous support and friendship.

Finally, I would like to thank my husband, Ahmad. His support, encouragement, patience and unwavering love have been undeniably my most invaluable asset for the past four years. I am grateful to him for the happiness and enjoyment he brought into my life.

To the memory of my father

Coherent Beam Combining for High Power Laser Applications

by Mercedeh Khajavikhan

ABSTRACT

This thesis is an effort to address several issues in coherent beam combining. First, a mathematical formalism is developed to study cavity dependent properties, in particular, the modal response of complex laser systems. It is shown that the coherent beam combining in these common cavities is extremely sensitive to random path-length variations of the individual gain elements.

Next, a number of methods are explored to reduce this sensitivity to length variations without actively controlling the path-lengths. This thesis introduces several coherent beam combining architectures based on Michelson cavity in which the spatial and longitudinal supermodes of the common cavity are manipulated to decrease the path-length sensitivity. A set of experiments is designed to verify the role of spatial and longitudinal supermodes. The measured dominant eigenmode, eigenvalue and output power are in good agreements with the predictions of the modal analysis.

Finally, many applications prefer the output power to be concentrated in a small spot, whereas the supermodes of most complex cavities contain several lobes. This thesis describes a mode shaping technique, capable of converting any supermode to the desired distribution, with theoretically a 100% efficiency. The technique employs two phase plates modifying the phases in Fourier conjugate planes to create a uniform beam (both in amplitude and phase), which directs all the power to the central lobe of the far-field. An experiment is performed to combine eleven in-phase beams, corresponding to the fundamental mode of the self-Fourier cavity, into a single-lobed far-field.

Contents

Acknowledgments	i
Dedication	iii
Abstract	iv
List of Tables	viii
List of Figures	ix
1 Introduction	1
2 Modal Study of Laser Common Cavities	7
2.1 Michelson Cavity	8
2.2 Dammann Grating Cavity	14
2.3 Volume Bragg Grating Cavity	16
2.4 Talbot Cavity	18
2.5 Self-Fourier Cavity	21
2.6 Parallel Waveguide Cavities	26
2.6.1 Weak Coupling Regime ($\alpha \ll 1$)	28
2.6.2 Strong Coupling Regime ($\alpha \rightarrow 1$)	30
2.7 Cavity Sensitivity to Random Path-length Variations	34
2.7.1 Beam-splitter Cavity	37
2.7.2 Dammann Grating Cavity	38

2.8	Conclusion	39
3	Modal-Based Sensitivity Reduction Techniques: Theory	42
3.1	Modal Analysis: Standard Michelson Cavity	43
3.2	Modal Analysis: Generalized Michelson Cavity	43
3.3	Radiance Improvement Using Spatial Supermodes	46
3.4	Radiance Improvement Using Longitudinal Modes	53
3.5	Conclusion	58
4	Modal-Based Sensitivity Reduction Techniques: Experiment	60
4.1	Experimental Considerations	61
4.2	Spatial Supermodes	65
4.2.1	Standard Michelson Cavity ($r_r = 0$)	65
4.2.2	Generalized Michelson Cavity ($r_r \neq 0$)	69
4.3	Longitudinal Modes	75
4.4	Conclusion	77
5	Mode Shaping	79
5.1	Beam Evaluation Parameters	80
5.1.1	Strehl Ratio	80
5.1.2	Overlap Ratio	81
5.1.3	Radiance and spectral radiance	81
5.1.4	Beam Quality factor (M^2)	82
5.2	Review of Mode-Shaping Techniques	82
5.3	Swanson Aperture Filling Technique	84
5.4	Generalized Amplitude-to-Phase Conversion	86
5.5	Experimental Results	89
5.6	Comparison: Dammann Grating and Aperture Filling Techniques	93

5.7 Conclusion	97
6 Conclusion and Discussion	99
References	102

List of Tables

5.1	Comparison between Swanson and Generalized Techniques	88
-----	---	----

List of Figures

1.1	Spectral and Polarization Beam Combining	2
1.2	MOPA and Common Cavity Architectures	4
2.1	Beam-Splitter Resonator (Standard Michelson Cavity)	10
2.2	Binary Tree and Linear Chain Structures	13
2.3	Dammann Grating Cavity	14
2.4	Triple Exposure Volume Bragg Grating	17
2.5	Volume Bragg Grating Cavity	18
2.6	Talbot Cavity	19
2.7	Self-Fourier Cavity	22
2.8	Modes of Self-Fourier Cavity	25
2.9	Parallel Waveguide Cavity	27
2.10	Modes of Weak Coupled Cavity	31
2.11	Error of Weak Coupled Cavity	32
2.12	Modes of Strong Coupled Cavity	35
2.13	Error of Strong Coupled Cavity	36
2.14	Phase-Error-Loss in Michelson Cavity	38
2.15	Phase-Error-Loss in Dammann Grating Cavity	40
3.1	Beam-Splitter Resonator	44
3.2	Phase-Error-Loss of Generalized Michelson Cavity	47
3.3	Output Power as a Function of Recycle Reflectivity	50
3.4	Average Power due to Output-Recycle Phase Mismatch	51
3.5	Output Power	53

3.6	Longitudinal Mode Dominated Regime	56
3.7	Comparison between Longitudinal and Spatial Regimes	57
3.8	Gradual Transition from Spatial to Longitudinal Regime	57
3.9	Averaged Normalized Output Power	58
4.1	Generalized Michelson Cavity	61
4.2	Polarization Multiplexed Cavity	63
4.3	Eigenmode of the Standard Michelson Cavity	66
4.4	Phase-error Loss of Standard Michelson Cavity	67
4.5	Output Power of Standard Michelson Cavity	68
4.6	Eigenmode of Generalized Michelson Cavity	70
4.7	Phase-error Loss of the Generalized Michelson Cavity	71
4.8	Output Power of the Generalized Michelson Cavity	71
4.9	Eigenmode of Generalized Michelson Cavity	73
4.10	Phase-error Loss of the Generalized Michelson Cavity	74
4.11	Output Power of the Generalized Michelson Cavity	74
4.12	Polarization Multiplexed Cavity with Walk-off Polarizer	75
4.13	Output Power	77
4.14	Comparison: Cold Cavity-Experiment	78
5.1	Superposition vs. Aperture Filling	83
5.2	Swanson's Technique	85
5.3	Example of Swanson's Technique	86
5.4	Grechburg-Saxton Algorithm	87
5.5	Generalized Technique	87
5.6	Experimental Set-up of generalized Technique	90
5.7	Experimental Results of Generalized Technique	91
5.8	Theory-Experiment Comparison	92
5.9	Superposition vs. Generalized Technique	94
5.10	Phase Plates Comparison	96
6.1	Combining Efficiency: Longitudinal	100
6.2	Combining Efficiency: Longitudinal and Spatial	101

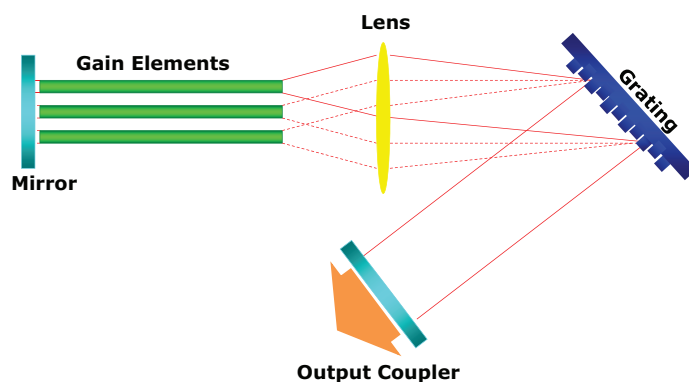
Chapter 1

Introduction

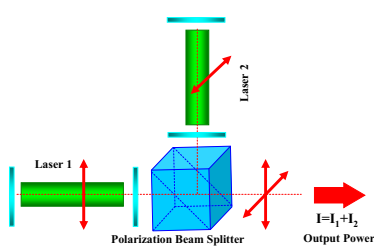
High radiance lasers have been utilized in numerous scientific and industrial applications, including such disparate fields as material processing, medical research, and particle acceleration. The radiance, defined in this thesis as the power per unit area per unit solid angle integrated over all wavelengths and both polarizations, directly relates to two of the laser characteristics: output power and beam quality. In many applications, radiance is the quantity of practical interest since it is directly proportional to the ability to concentrate power in the far field (or at the focal plane of a lens) from an optical system with a fixed aperture diameter. Pumping a gain-module more aggressively to achieve higher power does not necessarily improve the radiance. In fact, at higher pump power, the waste heat and high circulating optical power in a gain-module can trigger a number of undesirable thermal and nonlinear effects including depolarization, thermally induced aberrations, optical Kerr nonlinearities, optical damage, and several scattering mechanisms that eventually limit the maximum attainable radiance.

An alternative approach to resolve all the aforementioned problems is suggested by combining beams from several lower radiance elements. Using the above definition of radiance, it is clear that the radiance from mutually incoherent sources can be increased by multiplexing lasers of different spectral signatures

(spectral beam combining) [1] or by combining lasers with two orthogonal polarization states (polarization beam combining) [2]. Figures 1.1 a and b show configurations for spectral beam combining and polarization beam combining, respectively. Although these methods can be quite useful in a variety of applications, they degrade the spectral and polarization purity of the resulting output. In this thesis, we concentrate exclusively on coherent beam combining techniques where the spectral and polarization characteristics of the output beam are faithful reproductions of each of the input beams.



(a)



(b)

Figure 1.1: Architectures for (a) spectral and (b) polarization beam combining.

The first wave of interest in coherent beam combining emerged after the revolutionary advances in semiconductor lasers. Highly efficient monolithic arrays of semiconductor lasers offer ideal low power sources for beam-combining. A number of coupling mechanisms were devised to coherently combine the array elements, including evanescent coupling in index-guided laser arrays [3] and gain-guided arrays [4], leaky wave coupling in index-guided antiguide arrays [5], spatial filtering [6], [7], diffraction coupling in the form of Talbot self-imaging [8], [9], Dammann-grating-assisted beam combining [10], and self-Fourier cavities [11].

Recent advances in fiber lasers brought coherent beam combining into focus for the second time. In fiber lasers, the long length provides more amplification and simplifies pumping, the waveguiding effect improves the beam quality, and the high surface-to-volume ratio facilitates thermal management. At the same time, lengthy single-mode fiber lasers with their relatively small mode area are more susceptible to nonlinear complications. Therefore, although fiber lasers generally provide higher radiance in comparison with semiconductor lasers, they too have a practical radiance limit. Coherent beam combining may offer one of the few prescriptions to break through this radiance barrier limit.

To appreciate the coherent beam combining problem, it is instructive to assess the physical limits of beam combining dictated by the radiance theorem. Specifically, the radiance theorem implies that, given N uncorrelated modes, the power per mode cannot be increased by any optical system that is in thermal equilibrium (non-inverted medium). Since the fields from mutually incoherent lasers are uncorrelated, the light from an ensemble of these beams can be described as containing several modes, one from each laser. From the radiance theorem, the only way to increase the radiance beyond that of a single source is to reduce the number of modes in the system. The field radiance can therefore be maximized by forcing all the individual modes into a single coherent state by establishing a fixed (non-time-varying) phase relationship between each of the laser sources. The process of creating this new single mode is often referred to as establishing mutual coherence across the various laser sources.

There have been several optical methods proposed to achieve the mutual coherence required above [2]. One of the most straightforward is a Master-Oscillator-Power-Amplifier (MOPA) architecture, whereby a single coherent source is amplified by an array of gain elements [12, 13]. Mutual coherence results from coherent amplification of a common signal. Another approach employs some form of coupling between the laser elements to create a coupled oscillator. The light field from the coupled lasers then consists of a linear superposition of “supermodes”, corresponding to the specific normal modes of the coupled array. In this approach, coherence is established by providing mode-dependent cavity losses. If only one supermode is allowed to exceed threshold, the phases from all the lasers are locked together in a coherent state (described by this supermode). Of course, allowing additional modes to lase degrades the coherence; in the limit where all supermodes lase, the source can be considered to be totally mutually incoherent and no increase in radiance is possible. Thus, it is clear that the ability to discriminate between supermodes is an important attribute of the various cavity architectures. Figures 1.2 a and b show the two aforementioned coherence establishment techniques. In this thesis, we concentrate exclusively on coherent beam combining architectures based on common cavities.

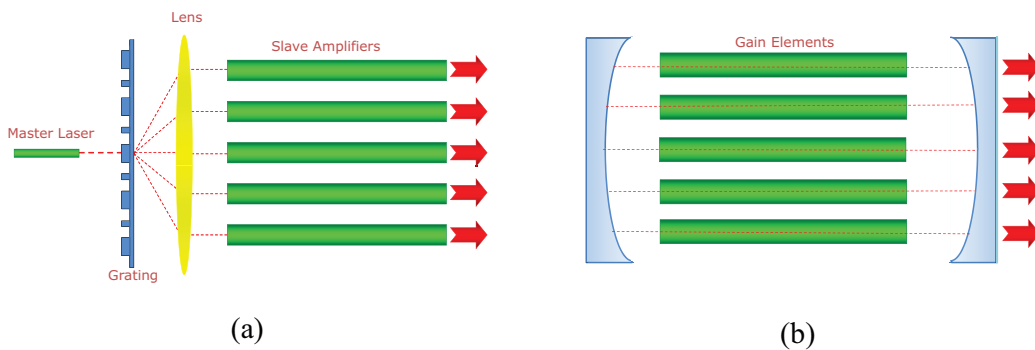


Figure 1.2: Architectures for coherence establishment. (a) Master Oscillator Power Amplifier (b) common cavity.

Chapter 2 employs a modal approach to study complex laser resonators (common cavities), including: beam-splitter resonator, Dammann grating cavity, volume grating cavity, Talbot cavity [16], self-Fourier [17], and parallel waveguide cavities. [3, 15].

Since coherent beam combining by nature is concerned with the field components of different laser beams, there is an inherent sensitivity to the specific phases presented by each beam. The phases of the individual beams in a real laser system can be influenced dramatically both by inadvertent changes in resonator path lengths as well as changes in the optical properties of the gain media. These path length errors across the laser array can lead to changes in the supermode field distribution, increased supermode losses, and reduced modal discrimination. In the final section of chapter 2 we calculate the effect of cavity path length errors on mode shape and loss for Michelson and Dammann grating cavities. We will see that understanding the effects of phase errors and controlling the individual laser phases is key to the successful implementation of coherent beam combining.

Chapter 3 introduces several passive techniques to reduce the sensitivity of the output radiance to random path-length changes. We focus on the modal characteristics exhibited by the Michelson-type cavities. This canonical model helps to understand the most fundamental properties of more complex common cavities. We observe that in the generalized Michelson cavity the additional supermodes permit one to trade modal discrimination for some degree of path-length tolerance. In the same manner, the longitudinal modes of the Michelson cavity can be engineered to improve the output radiance. Chapter 4 provides several experiments to challenge the path-length sensitivity reduction techniques developed in chapter 3.

Finally the above coherence requirement ensures that the power per mode increases as more lasing elements are added to the array. However, it does not necessarily ensure that the power per unit area per unit solid angle (the conventional definition of radiance) is optimum in any sense. To achieve this, the mode must be converted into the desired form by manipulating its intensity and phase.

The actual optimal shape is dependent on the particular application. To maximize conventional on-axis radiance, the field emanating from a finite-size aperture (containing the combined laser beams) must be coupled into a far-field delta function in an optimal manner. Because of the Fourier relationship between the near and far fields, the optimum near-field distribution is the one that approximates a plane wave over the extent of the lasing aperture. Thus, the mode should be converted into a shape that *uniformly* illuminates the optical aperture in amplitude and phase. If, on the other hand, one desires a mode with a low M^2 , the beam should be converted into a Gaussian distribution. There are many techniques to perform this conversion in a quasi-lossless manner by manipulating the phase of the beam in one or more locations [18]. This step is essential to achieve a useful output and true high radiance. Chapter 5 explains a technique to combine coherent beams into a desired shape with virtually 100% efficiency.

Chapter 2

Modal Study of Laser Common Cavities

This chapter provides a mathematical foundation for the study of common laser cavities. These cavities like other resonant structures, quantum wells and waveguides in lateral dimensions, operate in several discrete states known as eigenmodes. Given a linear transformation, an eigenfunction, also called eigenmode or eigenvector, is a nonzero function that may only change by a scalar when that transformation is applied. The scalar is called eigenvalue. Since the modes of the common cavity belong to the collective system, they are called supermodes to be distinguished from the Hermite Gaussian modes of single gain element lasers.

The eigenmodes are self-consistent circulating fields. As a result, they can be retrieved from the round-trip equation of the cavity. In forming the round-trip equation, depending on the accuracy required and the particular cavity under study, the cavity elements can be represented by the principles of the geometrical optics, wave optics, or even quantum optics. Since our goal is to provide an analytical, yet simple formalism that explains the most prominent properties, in most cases we apply geometrical and/or wave optics approximations.

The laser common cavity contains several gain elements that can modify the modal response. To a first approximation, the gain elements compensate the

modal loss and establish lasing condition by providing signal amplification. The effect of the gain element becomes more complicated considering its nonlinear properties. Our approach in this thesis is to determine the eigenmodes based on the cold cavity (cavity geometry and coupling between the gain elements), and allow the gain elements to modify the eigenvalues. This modification can be as simple as amplifying the eigenvalue to compensate the loss or it can be more subtle gain dependent effects like suppression of one or several modes due to spatial hole burning.

This chapter is organized as follows. Section 2.1 to 2.6 presents the modal characteristics of several common cavities including the Michelson cavity (section 2.1), Dammann grating cavity (section 2.2), volume Bragg grating cavity (section 2.3), Talbot cavity (section 2.4), self-Fourier cavity (section 2.5), and parallel waveguide cavities (section 2.6). Section 2.8 discusses the effect of random variations of the gain elements on the performance of common cavities. Section 2.9 is reserved for concluding remarks.

2.1 Michelson Cavity

Lasers can be coherently combined by the technique of beam superposition using an optical element that overlaps the fields of two or more beams while simultaneously converting the combined phase front into a uniform or quasi-uniform plane wave. Several simple demonstrations of coherent beam combining have utilized a simple beam splitter to form a Michelson resonator, shown schematically in fig. 2.1. In this section we study the modal properties of this resonator for coherent beam combining. Although most fiber-based systems have used a 50:50 beam coupler as shown in fig. 2.1(b) [19], we will describe the combining process using the equivalent cavity shown in fig. 2.1(a), where a properly coated dielectric slab acts as a beam-splitter. The gain elements are placed in the sections labeled arm 1 and arm 2, and the combined laser power is extracted through the mirror in the output arm. A beam block (BB) in the final port ensures that no light will return

from this arm of the beam splitter. Provided proper path lengths are established, this resonator coherently combines the power generated by the gain elements into a single, higher radiance beam exiting the output arm.

On a basic level, this structure can be understood by a simple application of the time reversal property. If, instead of the beam direction indicated in the figure, the original beam path consists of a single beam incident on the dielectric slab from the right-hand side (labeled output arm), a 50:50 beam splitter will split this beam into two equal intensity beams exiting ports at the bottom and the left (arms 1 and 2). These beams are phase-coherent and have a unique phase relationship. Therefore, by the time reversal property, two coherent beams with this same phase relationship can be combined in the manner illustrated in fig. 2.1(a).

Although this simple explanation justifies the basic operation, a more detailed description of the resonator characteristics requires a deeper understanding of its modal structure. This is provided by the eigenvalue equation describing light propagation inside the resonator. The round-trip propagation equation contains the effect of all the intervening optical elements encountered by the beam in one circulation around the cavity. Optical resonators, based on a round-trip self-replication condition, support a set of eigenmodes, each with its own corresponding eigenvalue. For the Michelson cavity, a matrix representation of the round-trip propagation equation leads to a particularly simple result, so that the eigenvalues and eigenvectors can be easily derived by algebraic techniques.

To construct the round-trip matrix we take two beams at particular points in the gain arms and propagate them around the cavity and back to the initial points of departure. Here we assume the beams begin their journey directly after reflection from the mirrors in the gain arms (a_{10} and a_{20} in fig. 1a). They then acquire specific phase shifts proportional to the optical path lengths as they travel along the gain arms (represented by matrix Φ), and are redirected by the beam-splitter into the upper and right resonator arms according to the beam splitter scattering matrix (S). The beam in the right-hand arm is reflected back by the

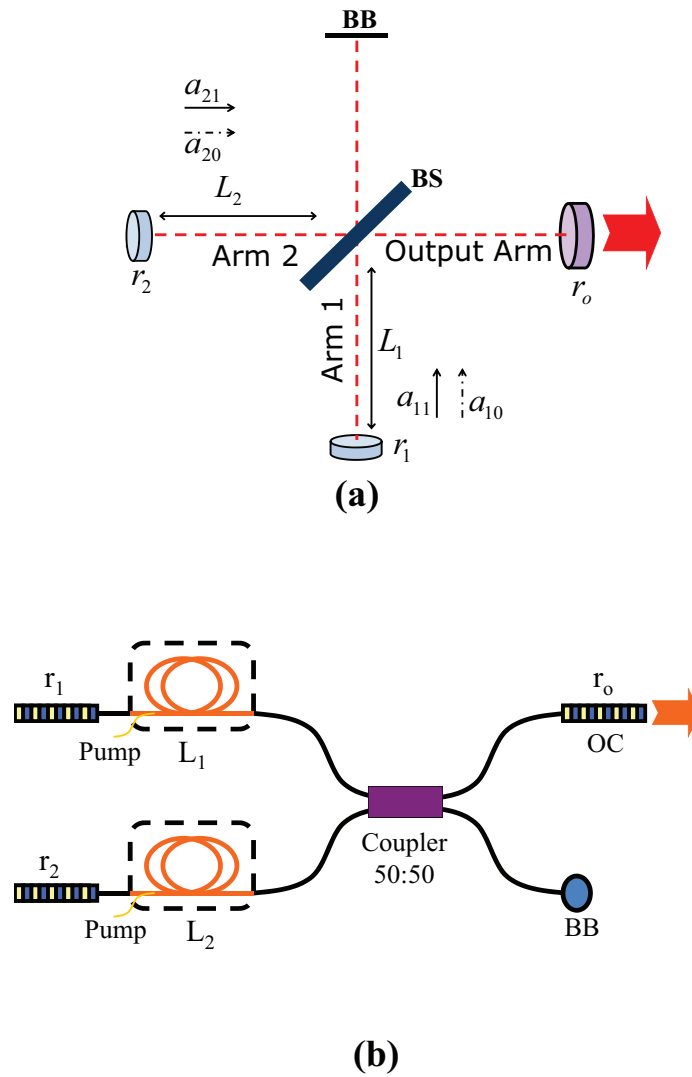


Figure 2.1: (a) Beam-splitter resonator with a beam-block in one arm (Michelson cavity). (b) The equivalent fiber-based cavity (the beam-splitter has been replaced by fiber coupler). BB: Beam-block, BS: beam-splitter. $L_{1,2}$: Lengths of the arms 1 and 2. a_{10} and a_{20} are initial fields, and a_{11} and a_{21} are same fields after one round-trip in the cavity.

mirror in the output arm (R), and is subsequently redirected by the beam-splitter into the left hand and lower resonator arms according to the transpose scattering matrix (S^T). The beam in the upper arm is absorbed by the beam block. The beams travel once more through the gain arms (Φ) to finally reach the points of departure after reflecting back by the mirrors (a_{11} and a_{21} in fig. 1a). The round-trip matrix of the cavity is a product of all these matrices:

$$M = \Phi S^T R S \Phi, \quad (2.1)$$

where

$$\Phi = \begin{pmatrix} e^{j\frac{\phi_1}{2}} & 0 \\ 0 & e^{j\frac{\phi_2}{2}} \end{pmatrix},$$

$$R = \begin{pmatrix} r_o & 0 \\ 0 & r_{bb} \end{pmatrix},$$

and $\phi_i = 2kL_i$, k is the wave number of the light, r_o is the amplitude reflectivity of the output mirror, and r_{bb} is the reflectivity of the beam block. The scattering matrix for a lossless and reciprocal beam-splitter (\mathbf{S}) is:

$$S = \begin{pmatrix} r & jt \\ jt & r \end{pmatrix}, \text{ where } r^2 + t^2 = 1. \quad (2.2)$$

In this scattering matrix, r is the amplitude reflectivity and t is the amplitude transmittivity of the beam-splitter. While the exact values of r and t depend on a particular beam splitter under study, fundamental properties govern the relationships between the elements of the matrix. For example, reciprocity requires a *symmetric* scattering matrix and a lossless beam-splitter requires a *unitary* matrix.

Assuming a 50:50 power beam-splitter with $r = t = 1/\sqrt{2}$ and a perfectly absorbing beam block ($r_{bb} = 0$), the round-trip matrix (M_{rt}) can be simplified to:

$$M_{rt} = \begin{pmatrix} \frac{1}{2}r_o e^{j\phi_1} & \frac{j}{2}r_o e^{j\frac{(\phi_1+\phi_2)}{2}} \\ \frac{j}{2}r_o e^{j\frac{(\phi_1+\phi_2)}{2}} & -\frac{1}{2}r_o e^{j\phi_2} \end{pmatrix}. \quad (2.3)$$

By noting the linear dependence between the two columns, it is easy to see that M_{rt} is rank one, meaning that it has only one non-zero eigenvalue. Physically, this corresponds to a resonator that supports only one supermode. This single eigenvector V and its corresponding eigenvalue λ can be expressed in a simple mathematical form:

$$V = \begin{pmatrix} \frac{1}{\sqrt{2}} \\ \frac{j}{\sqrt{2}} e^{j\frac{\Delta\phi}{2}} \end{pmatrix} \quad (2.4)$$

and

$$\lambda = -jr_o e^{j\frac{(\phi_2+\phi_1)}{2}} \sin\left(\frac{\Delta\phi}{2}\right), \text{ where } \Delta\phi = \phi_2 - \phi_1. \quad (2.5)$$

The previous architecture can be extended to combine more than two gain elements by a number of means. It is instructive to examine two straightforward extensions shown in fig. 2.2 for combining beams from four gain elements. The first architecture, shown in fig. 2.2(a), is a binary tree where each node of the tree is replaced by a beam-splitter. The second architecture consists of a linear chain of beam splitters. It is easy to show that both these architectures also support only a single supermode. This supermode can be designed to have equal light intensity in each gain arm by adjusting the splitting ratios of the beam splitters. The binary tree architecture requires all splitting ratios to be 50:50 whereas the beam splitting ratios of the linear chain are a function of position. In a manner similar to the simple Michelson resonator, the eigenvalue associated with each of these single mode cavities is a strong function of path length errors. However, a careful adjustment of the path-lengths results in no power loss in the arms with beam blocks.

The round-trip matrices of these resonators can be formed by properly multiplying the scattering matrices of the individual elements. The eigenvalues and eigenmodes can be simply deduced from the eigen-equation.

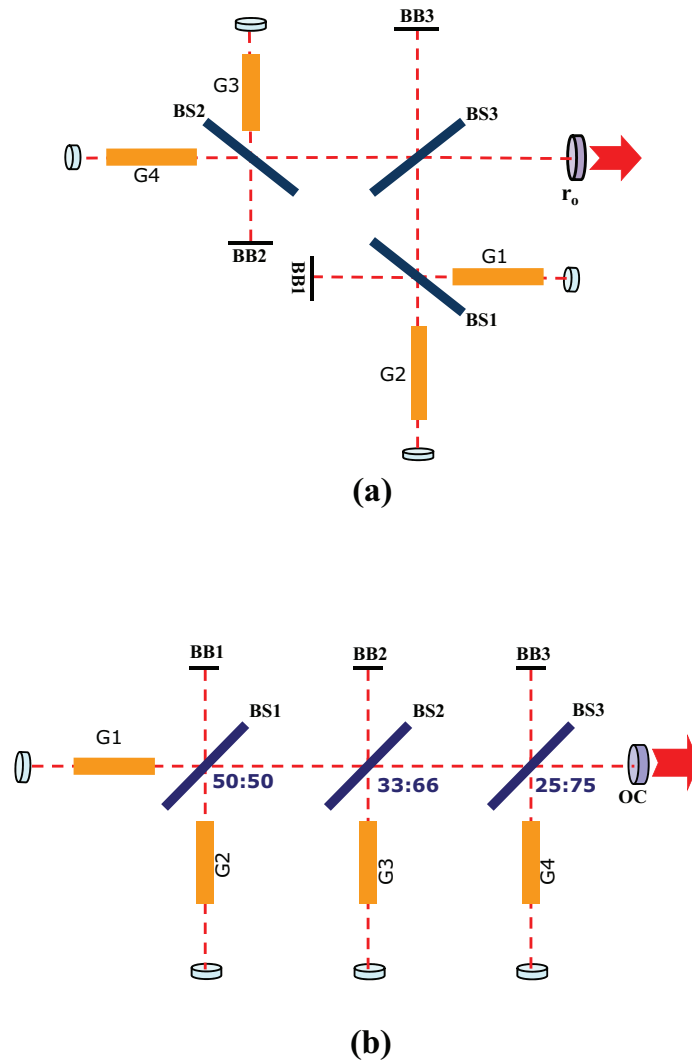


Figure 2.2: (a) Binary-tree configuration to combine four gain elements. All beam-splitters are 50:50. (b) Linear-chain configuration to combine four gain elements. The beam-splitters are from left to right 50:50, 66:33, and 75:25. BB: beam-block, OC: output coupler, BS: beam-splitter, G1-G4: gain elements.

2.2 Dammann Grating Cavity

A more practical method of combining multiple beams (shown in fig.2.3) utilizes a single Dammann grating [21], [34]. This device essentially acts as a multi-arm beam splitter by efficiently splitting a single incident beam into N beams of approximately equal intensities. Each order of the grating is equivalent to a port in a conventional beam-splitter. The scattering matrix for a perfect six-port splitter (three input ports and three output ports), derived with the help of the properties of lossless, reciprocal and time reversible systems, is given by

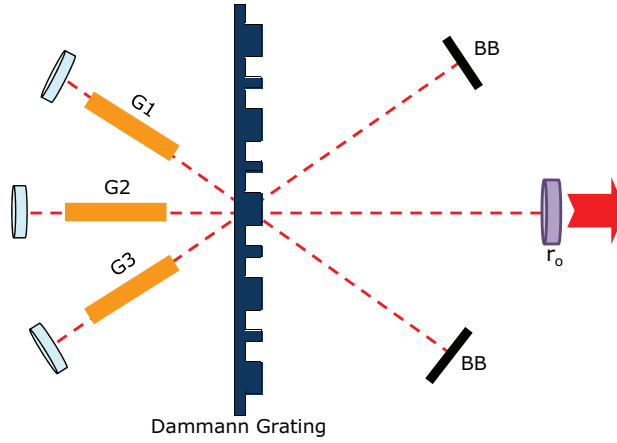


Figure 2.3: Dammann grating cavity. BB: beam-block, OC: output coupler, G1-G3: gain elements.

$$S = \begin{pmatrix} \frac{1}{\sqrt{3}} & \frac{1}{\sqrt{3}}e^{j\frac{2\pi}{3}} & \frac{1}{\sqrt{3}}e^{j\frac{2\pi}{3}} \\ \frac{1}{\sqrt{3}}e^{j\frac{2\pi}{3}} & \frac{1}{\sqrt{3}} & \frac{1}{\sqrt{3}}e^{j\frac{2\pi}{3}} \\ \frac{1}{\sqrt{3}}e^{j\frac{2\pi}{3}} & \frac{1}{\sqrt{3}}e^{j\frac{2\pi}{3}} & \frac{1}{\sqrt{3}} \end{pmatrix}. \quad (2.6)$$

In general, the scattering matrix of an $N \times N$ Dammann grating must have the following properties:

$$|s_{ij}| = \frac{1}{\sqrt{N}}$$

$$s_{ij} = s_{ji}$$

$$\text{Row}(i) \cdot \text{Row}(j) = \begin{cases} 0 & i \neq j \\ 1 & i = j \end{cases}$$

Back to the 3×3 Dammann grating, the round-trip matrix of the Dammann grating cavity is given by

$$M_{rt} = \frac{1}{3} r_o \begin{pmatrix} e^{j\frac{4\pi}{3}} e^{j\phi_1} & e^{j\frac{2\pi}{3}} e^{j\frac{\phi_1+\phi_2}{2}} & e^{j\frac{4\pi}{3}} e^{j\frac{\phi_1+\phi_3}{2}} \\ e^{j\frac{2\pi}{3}} e^{j\frac{\phi_1+\phi_2}{2}} & e^{j\phi_2} & e^{j\frac{2\pi}{3}} e^{j\frac{\phi_2+\phi_3}{2}} \\ e^{j\frac{4\pi}{3}} e^{j\frac{\phi_1+\phi_3}{2}} & e^{j\frac{2\pi}{3}} e^{j\frac{\phi_2+\phi_3}{2}} & e^{j\frac{4\pi}{3}} e^{j\phi_3} \end{pmatrix}. \quad (2.7)$$

Similar to the Michelson cavity, the round trip matrix is of unity rank, indicating the existence of a single spatial supermode. The eigenvector V and eigenvalue λ associated with this supermode are given by

$$V = \begin{pmatrix} \frac{1}{\sqrt{3}} e^{j\frac{(\phi_1-\phi_2)}{2}} e^{j\frac{2\pi}{3}} \\ \frac{1}{\sqrt{3}} \\ \frac{1}{\sqrt{3}} e^{j\frac{(\phi_3-\phi_2)}{2}} e^{j\frac{2\pi}{3}} \end{pmatrix} \quad (2.8)$$

and

$$\lambda = \frac{r_o}{3} e^{j\frac{4\pi}{3}} e^{j\phi_2} \left\{ e^{j(\Delta\phi_1)} + e^{j\frac{2\pi}{3}} + e^{j(\Delta\phi_3)} \right\}; \Delta\phi_i = \phi_i - \phi_2. \quad (2.9)$$

The design of a 100% efficient Dammann grating with only three orders can be quite challenging. The optimum phase profile for the Dammann grating is found by applying appropriate numerical techniques [23], [24]. The algorithm is extensively explained in chapter 5. From the resulting profile distribution, the scattering matrix of the Dammann grating is calculated. The elements of the scattering matrix are found by emanating a known field to one of the input arms of the grating and measuring the magnitude and phase of the resulting fields

coupled to each of the output arms. In the design of this grating it is assumed that the grating supports only 3 propagating orders (the rest of the orders are evanescent). The scattering matrix of the designed Dammann grating is given by

$$S = \begin{pmatrix} 0.5753 \exp\{j0\} & 0.5705 \exp\{j2.0993\} & 0.5774 \exp\{j2.1013\} \\ 0.5705 \exp\{j2.0993\} & 0.5774 \exp\{j.0010\} & 0.5753 \exp\{j2.0993\} \\ 0.5774 \exp\{j2.1013\} & 0.5753 \exp\{j2.0993\} & 0.5705 \exp\{j0\} \end{pmatrix} \quad (2.10)$$

Since this scattering matrix closely resembles the scattering matrix of the ideal Dammann grating, the eigen-solution of the ideal Dammann cavity well approximates the eigenmode and eigenvalue of the practical Dammann cavity.

2.3 Volume Bragg Grating Cavity

Another practical method of combining multiple beams utilizes a volume Bragg grating in the cavity. Thick holographic gratings are often employed to produce high diffraction efficiency in the first order. If several strong diffraction orders are desired, as in the case of a multiple-beam splitter or a multiple-beam combiner, several fringe structures must exist simultaneously within the same emulsion.

For six port combiner/splitter equivalent to the Dammann grating in fig. 2.3, a triple-exposure grating structure is formed by incoherently superimposing three gratings within a single emulsion as shown in fig. 2.4. In writing this grating first, plane waves w_1 and w_2 , then, plane waves w_3 and w_2 , and finally plane waves w_1 and w_3 interfere in the emulsion. The interference patterns modulate the refractive index to create a phase-only structure. If written properly, the resulting volume Bragg grating equally splits an input beam, emanating parallel to any of the three writing beams (w_1, w_2, w_3), to three output orders again in the directions of the writing beams (w_1, w_2, w_3).

The grating is recorded by the interference of w_2 at normal angle and w_1 and w_3 at angles $\phi_{21} = \phi_{23} = \pi/3$. The modulation depths of the gratings recorded by

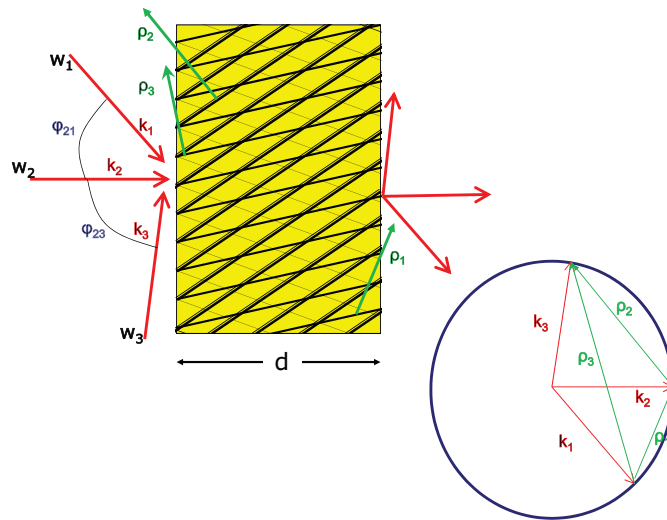


Figure 2.4: On the left: triple exposure volume Bragg grating (VBG), on the right: Bragg diagram for incoherently superimposed gratings with a common Bragg angle.

interference of w_1 and w_2 , and w_2 and w_3 are $\sqrt{2}$ times the grating recorded by the interference of w_1 and w_3 . This grating splits the applied input beam at the directions of either w_1 and w_2 and w_3 equally among the three output ports. Of course this condition is only satisfied at a particular thickness (d). In this case, the scattering matrix of the three-exposure grating is similar to the scattering matrix of the Dammann grating of the previous section.

$$S = \frac{1}{\sqrt{3}} \begin{pmatrix} 1 & e^{j\frac{2\pi}{3}} & e^{j\frac{2\pi}{3}} \\ e^{j\frac{2\pi}{3}} & 1 & e^{j\frac{2\pi}{3}} \\ e^{j\frac{2\pi}{3}} & e^{j\frac{2\pi}{3}} & 1 \end{pmatrix} \quad (2.11)$$

Figure 2.5 shows the volume grating cavity where the volume grating provides the coupling.

Dammann grating and volume Bragg grating cavities differ in the physical mechanism that causes the coupling between cavity elements. However, since the

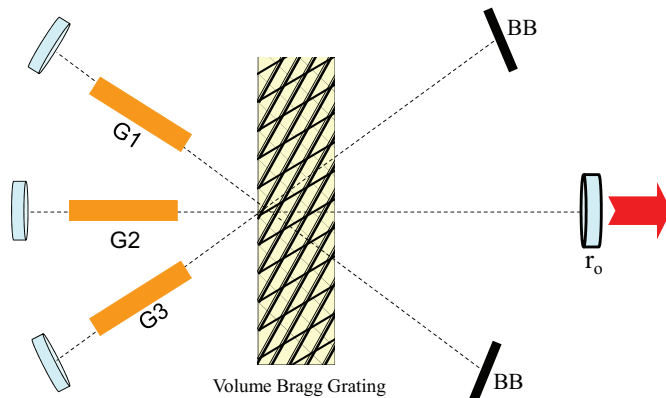


Figure 2.5: Volume Bragg grating cavity. BB: beam-block, OC: output coupler, G1-G3: gain elements.

scattering matrices of these cavities are identical, their eigenvalues and eigenvectors become identical, too.

2.4 Talbot Cavity

When a laterally periodic wave distribution is incident upon a periodic structure, its image is repeated at regular distances away from the plane. The regular distance is called the Talbot Length, and the repeated images are called self images or Talbot images. Furthermore, at half the Talbot length, a self image also occurs, but phase-shifted by half a period (the physical meaning of this is that it is laterally shifted by half the width of the period). At smaller regular fractions of the Talbot Length, sub-images can also be observed. At one quarter of the Talbot Length, the self image is halved in size, and appears with half the period of the grating (thus twice as many images are seen). At one eighth of the Talbot length, the period and size of the images is halved again, and so forth creating a pattern

of sub images with ever decreasing size.

The self-replicating property of the Talbot array is utilized to design a common cavity architecture known as Talbot cavity. The coupling is provided by Fresnel diffraction and it couples more strongly to the nearest neighbor. Figure 2.6 shows the Talbot cavity.

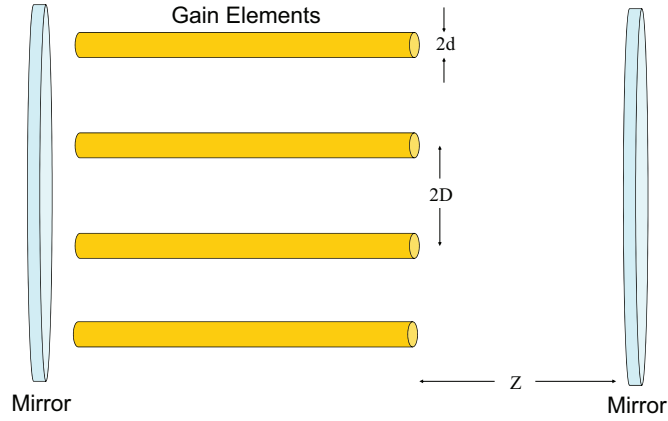


Figure 2.6: Talbot Cavity.

A simple treatment of the Talbot cavity assumes the elements of the array are delta-functions. In this case, the field distribution $p(x)$, at the right side of the gain elements is given by

$$p(x) = \sum_{i:\text{odd}} U_i^+ \delta(x - iT), \quad (2.12)$$

where U_i 's are the complex amplitude of the individual beams. After reflection upon the right mirror, the field distribution at the same location as $p(x)$, directing in the opposite direction is given by

$$q(x) = \frac{-j}{\sqrt{\lambda z}} \exp\{jkz\} \sum_{i:\text{odd}} U_i^+ \exp\left\{-j\pi T^2 \frac{(i-k)^2}{\lambda z}\right\}. \quad (2.13)$$

The round-trip matrix of this cavity is given by

$$\begin{pmatrix} \vdots \\ U_{-3}^+ \\ U_{-1}^+ \\ U_1^+ \\ U_3^+ \\ \vdots \end{pmatrix} = M_{rt} \begin{pmatrix} \vdots \\ U_{-3}^+ \\ U_{-1}^+ \\ U_1^+ \\ U_3^+ \\ \vdots \end{pmatrix} \quad (2.14)$$

$$M(m, n) = \frac{-j}{\lambda z} \exp\{jkz\} \exp\{-j\pi \frac{T^2(m-n)^2}{\lambda z}\} \exp\{j(\phi_m + \phi_n)\}, \quad (2.15)$$

where $\phi_i = 2kL_i$.

This round-trip matrix suggests that the full-Talbot cavity ($z = z_T = \frac{2T^2}{\lambda}$), supports two degenerate supermodes including the in-phase and out-of-phase modes. The lobes of the in-phase mode have identical phase, whereas in the out-of-phase mode every two adjacent lobes are π radians out of phase. Apparently, achieving coherence with the full Talbot cavity that supports two degenerate mutually incoherent modes is impossible. The half-Talbot cavity ($z = \frac{z_T}{2}$), on the other hand, only supports the out-of-phase supermode and therefore, may find applications in coherent beam combining.

The eigenmode and eigenvalue of the half-Talbot cavity, under this delta-function approximation, are given by

$$V = \begin{pmatrix} \vdots \\ \frac{-1}{\sqrt{N}} e^{j\frac{\phi_{-3}}{2}} \\ \frac{1}{\sqrt{N}} e^{j\frac{\phi_{-1}}{2}} \\ \frac{-1}{\sqrt{N}} e^{j\frac{\phi_1}{2}} \\ \frac{1}{\sqrt{N}} e^{j\frac{\phi_3}{2}} \\ \vdots \end{pmatrix} \quad (2.16)$$

$$\lambda = \frac{1}{N} (\dots + e^{j\phi_{-3}} + e^{j\phi_{-1}} + e^{j\phi_1} + e^{j\phi_3} + \dots), \quad (2.17)$$

where $N \rightarrow \infty$. It should be noted that the delta-function approximation is only valid when the cross section of each gain element is much smaller than the distance between them (extremely low fill-factor). Under this approximation, the number of modes supported by the full-Talbot and half-Talbot cavities are essentially independent of the number of the gain elements.

A more sophisticated treatment of the Talbot cavity assumes that the gain elements support Gaussian beams. The Gaussian beams undergo Fresnel propagation for $Z_T/2$ ($Z_T/4$ to the mirror and $Z_T/4$ back to the array), and couple to the gain elements. In this case, the elements of the round-trip matrix are given by:

$$M(m, n) = A \exp\left\{-\pi \frac{T^2(m-n)^2}{4d^4 + (\lambda z)^2}\right\} \exp\left\{-j\pi \frac{T^2(m-n)^2}{4d^4 + (\lambda z)^2}\right\} \exp\{j(\phi_m + \phi_n)\} \quad (2.18)$$

When the array fill factor is small ($d/T \ll 1$) and the number of the gain elements (N) is large, the full-Talbot cavity ($z = Z_T$) still supports two degenerate supermodes and the half-Talbot cavity ($z = Z_T/2$) supports only one supermode. However, as the number of gain elements reduces and the array fill factor (d/T) increases, the cavity starts to support more modes. In the limit of $d/T \rightarrow 1$, the Talbot cavity can be approximated with a parallel waveguide in the weak coupling regime. An approximate analytical solution for eigenvalues and eigenvectors of the cavity is presented in section 2.6.1.

2.5 Self-Fourier Cavity

The self-Fourier cavity, first proposed by Corcoran et. al., in one round-trip, performs Fourier transform on the initial field distribution. The mode of the self-Fourier cavity is identical to its Fourier transform. While many functions can be identified to have the self-Fourier property, the mode of Corcoran's cavity is composed of Gaussian beams with an overall Gaussian envelope [11]. Figure 2.8 illustrates the coupling mechanism between the gain elements in the self-Fourier

cavity. Unlike the nearest neighbor coupling mechanism in Talbot cavity, elements of the self-Fourier array all couples strongly to the central element.

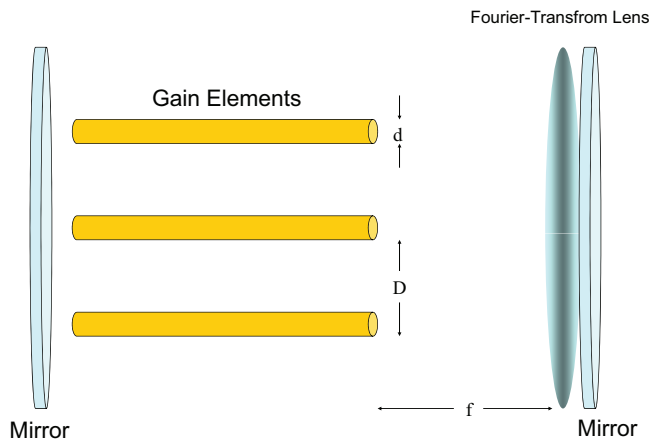


Figure 2.7: Self-Fourier Cavity.

The coupling matrix of the self-Fourier cavity relates the field distribution propagating to the right ($g(x)$) to the the field ($q(x)$), at the same location, propagating to the left after diffraction by the lens and reflection by the mirror. The initial field ($g(x)$), assuming gain elements support Gaussian beams with complex amplitudes of U_{i0} is given by

$$g(x) = \left\{ \dots + U_{-10} e^{-\pi \left(\frac{x-2D}{d}\right)^2} + U_{00} e^{-\pi \left(\frac{x}{d}\right)^2} + U_{10} e^{-\pi \left(\frac{x+2D}{d}\right)^2} + \dots \right\} e^{-\pi \left(\frac{y}{d}\right)^2}, \quad (2.19)$$

where $d/\sqrt{\pi}$ is the beam waist of the individual Gaussians, $2D$ is the distance between the neighboring beams, and U_i is the magnitude of the individual Gaussian beams. The lens located a focal length away from the array followed by the folding mirror, generates the far-field diffraction at the same location as $g(x)$. The resulting field ($q(x)$) is

$$q(x) = \frac{\sqrt{\pi}d}{j\lambda f} e^{-\pi(\frac{dx}{\lambda f})^2} \left\{ \dots + U_{-10} e^{-j2\pi\frac{2Dx}{\lambda f}} + U_{00} + U_{10} e^{+j2\pi\frac{2Dx}{\lambda f}} \right\}. \quad (2.20)$$

The field $q(x)$ then couples to the gain elements. The overlap integral below calculates the field coupling into each of the gain modules.

$$\frac{\int p(x)q(x)^* dx}{\sqrt{\int |p(x)|^2 dx} \sqrt{\int |q(x)|^2 dx}} \quad (2.21)$$

The coupling matrix relating $g(x)$ and $q(x)$ is then given by

$$\begin{pmatrix} \vdots \\ U_{-1}^- \\ U_0^- \\ U_1^- \\ \vdots \end{pmatrix} = M_{rt} \begin{pmatrix} \vdots \\ U_{-1}^+ \\ U_0^+ \\ U_1^+ \\ \vdots \end{pmatrix} \quad (2.22)$$

$$M(m, n) = \frac{\sqrt{2\pi\lambda f d}}{\sqrt{\pi^2 d^4 + (\lambda f)^2}} \exp \left\{ -\pi \frac{(N - 2m + 1)^2 + (N - 2n + 1)^2}{d^4 \pi^2 + (\lambda f)^2} - 2\pi j \frac{D^2 \lambda f (N - 2m + 1)(N - 2n + 1)}{d^4 \pi^2 + (\lambda f)^2} \right\}.$$

In addition, since the length of the gain elements are different, the individual beams acquire different phase shifts as they travel along the gain elements. The scattering matrix Φ gives the relative phase shift of the beams

$$\Phi = \begin{pmatrix} \ddots & & & & \\ & e^{j\frac{\phi_{-1}}{2}} & 0 & 0 & \\ & 0 & e^{j\frac{\phi_0}{2}} & 0 & \\ & 0 & 0 & e^{j\frac{\phi_1}{2}} & \\ & & & & \ddots \end{pmatrix}.$$

Given this phase error matrix, the round-trip matrix of the cavity is

$$M_{rt}(m, n) = \frac{\sqrt{2\pi\lambda f d}}{\sqrt{\pi^2 d^4 + (\lambda f)^2}} \exp\left\{-\pi \frac{(N - 2m + 1)^2 + (N - 2n + 1)^2}{d^4 \pi^2 + (\lambda f)^2}\right. \\ \left. - 2\pi j \left(\frac{D^2 \lambda f (N - 2m + 1)(N - 2n + 1)}{d^4 \pi^2 + (\lambda f)^2} + (\phi_m + \phi_n)\right)\right\} \quad M_{rt} = \Phi M \Phi$$

If the cavity is designed such that $(2D)^2 = \lambda f$ and $\pi d \ll D$, the rank of the round-trip matrix M_{rt} becomes 1. The eigenvector associated with this round-trip matrix is then, given by

$$V = \frac{v_i}{|V|}; \quad v_i = \exp\left\{j \frac{\phi_i}{2}\right\} \exp\left\{-\pi \frac{(N - 2i + 1)^2}{d^4 \pi^2 + (\lambda f)^2}\right\}. \quad (2.23)$$

Under this condition, the matrix has only one non-zero eigenvalue equal to the trace of the round-trip matrix.

$$\lambda = \sum_{i=1}^N M_{rt}(i, i) = \frac{\sqrt{2\pi\lambda f d}}{\sqrt{\pi^2 d^4 + (\lambda f)^2}} \sum_{i=1}^N \exp\{j\phi_i\} \exp\left\{-2\pi \frac{(N - 2i + 1)^2}{d^4 \pi^2 + (\lambda f)^2}\right\} \quad (2.24)$$

When the lengths of the array elements are adjusted such that their relative phase is zero ($\exp\{j\phi_i\} = 1$), the eigenvalue is maximum. Deviation from this ideal path-length condition directs some of the power to the higher order and, while the laser remains single mode, the eigenvalue become smaller.

The eigenmodes of the self-Fourier cavity are depicted in fig. 2.8. Since the cavity assumes to contain 7 gain elements, 7 degrees of freedom (seven modes) are resulted. However, as it can be seen in the figure the eigenvalues of all but the the first mode are vanishingly small.

It should be noted that the self-Fourier function is unlimited spanning from $-\infty$ to ∞ . In practice, the cavity limits to a finite number of gain elements.

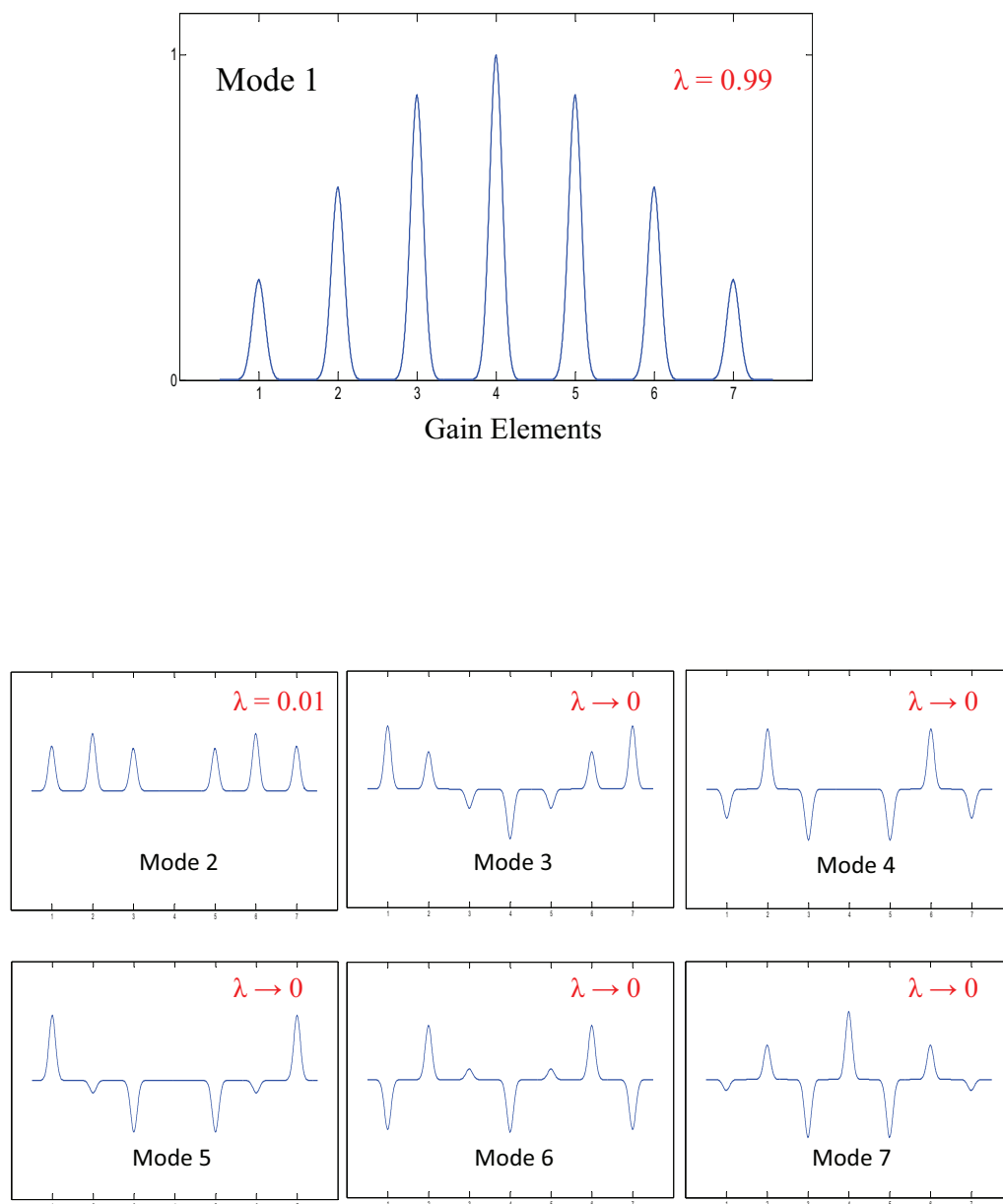


Figure 2.8: Modes of the self-Fourier cavity.

2.6 Parallel Waveguide Cavities

The parallel waveguide laser arrays and their application in coherent beam combining have been extensively explored over the last twenty years. Unlike the other beam combining common cavity architectures described in the preceding sections, we assume the form of the round trip matrix of this class of cavities is known. Here our effort concentrates on finding analytical solutions for the eigenmodes and eigenvalues.

According to [15], the coupling matrix of the parallel waveguide cavity is matrix M as given below.

$$\begin{pmatrix} \vdots \\ U_{11} \\ U_{21} \\ U_{31} \\ \vdots \end{pmatrix} = M \begin{pmatrix} \vdots \\ U_{10} \\ U_{20} \\ U_{30} \\ \vdots \end{pmatrix}; \quad M_{ij} = \alpha^{|i-j|} \quad (2.25)$$

where α is the coupling coefficient between the neighboring elements of the array. Since $|\alpha|$ is always smaller than one, the coupling strength between the elements decreases with the distance between them. Matrix M belongs to a family of matrices known as Toeplitz. A variety of physical phenomena may cause the array elements to couple with this characteristics. In particular, evanescent wave coupling in the index and gain guided semiconductor laser arrays results in similar matrices. While there is no exact analytical solution for eigenmodes and eigenvalues of this coupling matrices, sections 2.10 a and b describe approximate analytical solutions under weak and strong coupling conditions. In the weak coupling regime the field in each waveguide interacts weakly with the fields in other waveguides, whereas in the strong coupling regime, the interaction is strong. Figures 2.9 a and b show weakly and strongly coupled cavities, respectively.

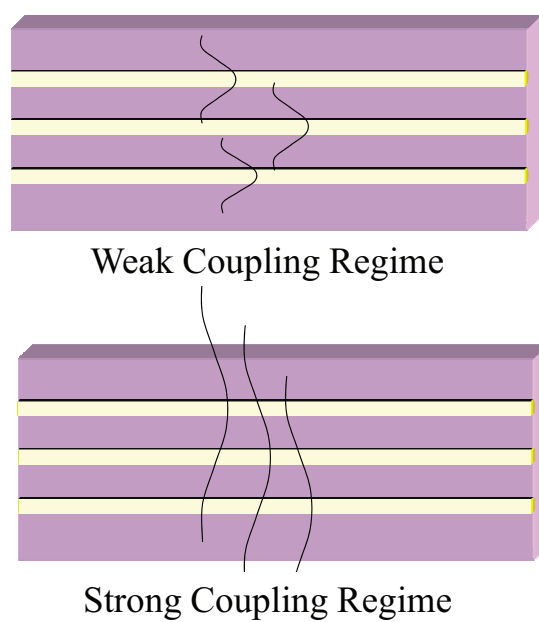


Figure 2.9: Parallel waveguide cavity. The cleaved surfaces provide the reflectivity.

2.6.1 Weak Coupling Regime ($\alpha \ll 1$)

The weak coupling regime mostly observed in evanescently coupled laser arrays. It is also a good approximation of the Talbot cavity with high fill factor. Equation 2.26 defines the eigenvalues and eigenvectors of the Toeplitz matrix, under the weak coupling regime. The columns of matrix \mathbf{S} are the eigenvectors of M and λ 's are the eigenvalues.

$$\mathbf{S}^T \mathbf{M} \mathbf{S} = \begin{pmatrix} \lambda_1 & & & & \\ & \lambda_2 & & & \\ & & \lambda_3 & & \\ & & & \ddots & \\ & & & & \lambda_n \end{pmatrix} \quad (2.26)$$

Applying the inverse operator on both sides of 2.26 yields 2.27.

$$\mathbf{S}^{-1} \mathbf{M}^{-1} (\mathbf{S}^T)^{-1} = \begin{pmatrix} \lambda_1^{-1} & & & & \\ & \lambda_2^{-1} & & & \\ & & \lambda_3^{-1} & & \\ & & & \ddots & \\ & & & & \lambda_n^{-1} \end{pmatrix} \quad (2.27)$$

Equation 2.28 defines the inverse of this Toeplitz matrix.

$$\mathbf{M}^{-1} = \begin{pmatrix} 1 & -\alpha & 0 & & 0 \\ -\alpha & 1 + \alpha^2 & -\alpha & 0 & \\ 0 & -\alpha & 1 + \alpha^2 & -\alpha & 0 \\ & & & \ddots & \\ & & 0 & -\alpha & 1 + \alpha^2 & -\alpha \\ 0 & & & 0 & -\alpha & 1 \end{pmatrix} \quad (2.28)$$

Then we define matrices \mathbf{B} and \mathbf{R} as given below.

$$\mathbf{B} = \begin{pmatrix} 0 & 1 & 0 & & 0 \\ 1 & 0 & 1 & 0 & \\ 0 & 1 & 0 & 1 & 0 \\ & & & \ddots & \\ & & 0 & 1 & 0 & 1 \\ 0 & & 0 & 1 & 0 \end{pmatrix} \quad (2.29)$$

and

$$\mathbf{R} = \begin{pmatrix} 1 & 0 & 0 & & 0 \\ 0 & 0 & 0 & 0 & \\ 0 & 0 & 0 & 0 & 0 \\ & & & \ddots & \\ & & 0 & 0 & 0 & 0 \\ & 0 & 0 & 0 & 0 & 0 \\ 0 & & 0 & 0 & 1 \end{pmatrix} \quad (2.30)$$

Therefore:

$$\mathbf{M}^{-1} = \frac{1 + \alpha^2}{1 - \alpha^2} \mathbf{I} + \frac{-2\alpha}{1 - \alpha^2} \mathbf{B} + \frac{\alpha^2}{1 - \alpha^2} \mathbf{R} \quad (2.31)$$

Where \mathbf{I} is the identity matrix.

Matrix \mathbf{R} approaches a null matrix when $\alpha \rightarrow 0$. Therefore, in the weak coupling regime, the eigenvectors of \mathbf{B} approximately diagonalize the round trip matrix \mathbf{M} . The eigenvalues of \mathbf{B} obey the iterative equation 2.32 that describes the Chebyshev polynomials of the second kind.

$$\mu f_i(\mu) = f_{i+1}(\mu) + f_{i-1}(\mu) \quad (2.32)$$

The solution of the above equation is

$$\mu_i = 2 \cos \left(\frac{i\pi}{N+1} \right) \quad (2.33)$$

\mathbf{V} in equation 2.34 shows the matrix of eigenvectors of \mathbf{B} , whose columns therefore approximately diagonalize the round trip matrix \mathbf{M} .

$$V = [v_{ik}]; v_{ik} = \sqrt{\frac{2}{N+1}} \sin\left(\frac{\pi}{N+1} ik\right) \quad (2.34)$$

Equations 2.27 and 2.31 and 2.33 are exploited to calculate the eigenvalues of the round trip matrix

$$\lambda_i = \frac{1 - \alpha^2}{1 + \alpha^2 - 2\alpha \cos\left(\frac{\pi i}{N+1}\right)} \quad (2.35)$$

Finally equation 2.31 describes how the eigenvector transformation affects \mathbf{R} .

$$(V^T R V)_{ik} = \begin{cases} 0 & i + j \text{ is odd} \\ \frac{4\alpha^2}{(1-\alpha^2)(N+1)} \sin\left(\frac{\pi i}{N+1}\right) \sin\left(\frac{\pi k}{N+1}\right) & i + j \text{ is even} \end{cases} \quad (2.36)$$

Under the conditions where $N \rightarrow \infty$ or $\alpha \rightarrow 0$, the error is negligible. Figure 2.10 compares the approximate eigenvalues and eigenvectors under the weak coupling condition with their numerically calculated counterparts.

Figures 2.11 a and b show the error as a function of the coupling coefficient (α) and the number of elements (N), respectively. We evaluate the relative root mean square error for the difference between the fundamental mode and the second highest mode. The plots confirm that for $N \rightarrow \infty$ or $\alpha \rightarrow 0$ the error is negligible.

The experiments with index guided semiconductor laser arrays recognizes the out-of-phase mode as the fundamental mode. In [], this contradiction between the theory and the experimental result is attributed to the loss between the gain elements. Since the in-phase mode, in comparison to the out-of-phase mode, contains stronger fields between the gain elements, it attenuates more strongly. The cavity's preference to oscillate in the out-of-phase mode can also be explained if the coupling coefficient is considered to be a negative number ($-1 < \alpha < 0$).

2.6.2 Strong Coupling Regime ($\alpha \rightarrow 1$)

The coupling coefficient in the strong coupling regime approaches unity. This leads to new set of matrices in equation 2.31. Equations 2.37 and 2.38 define

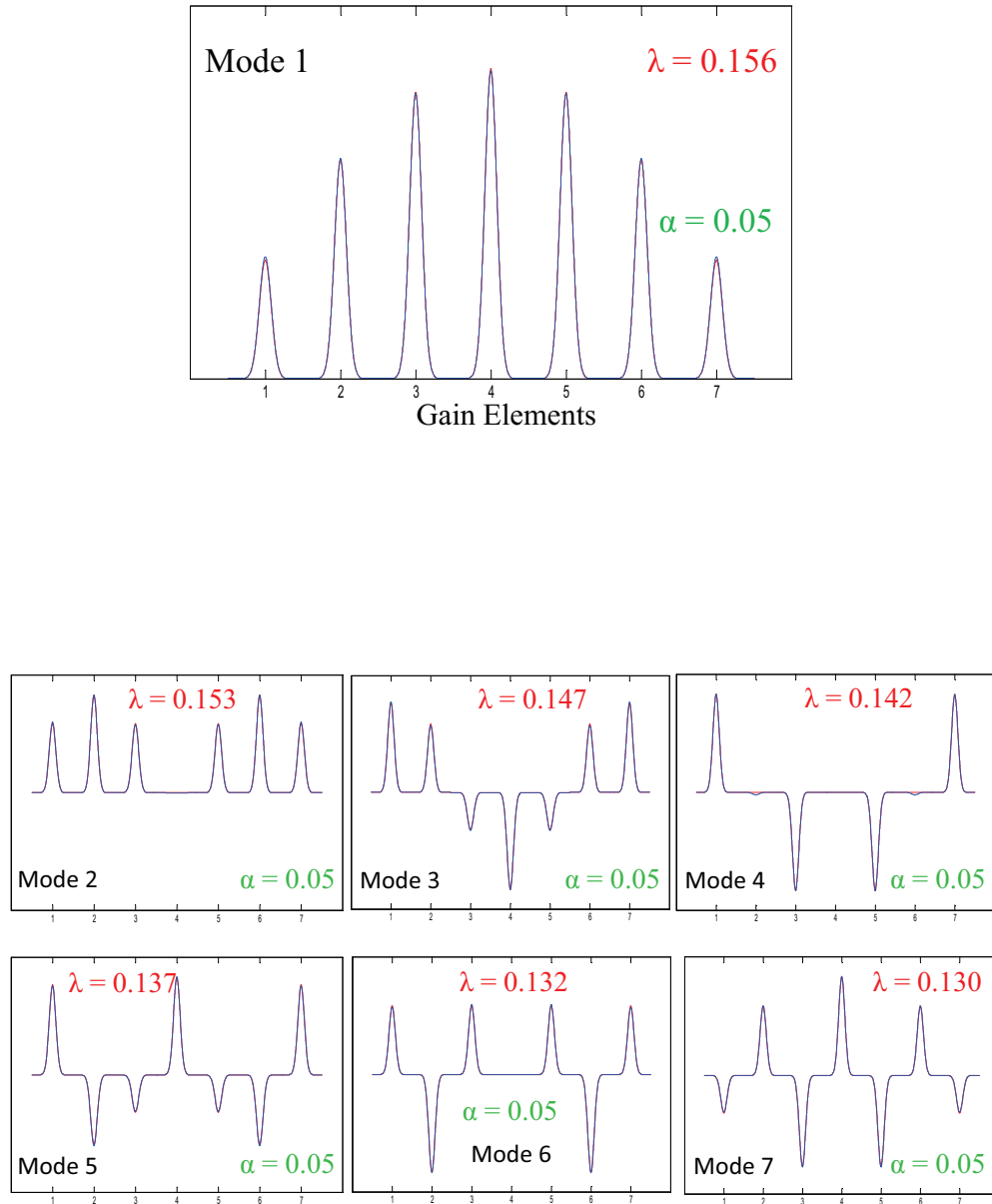
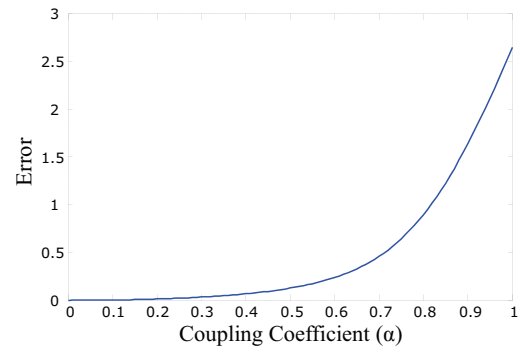
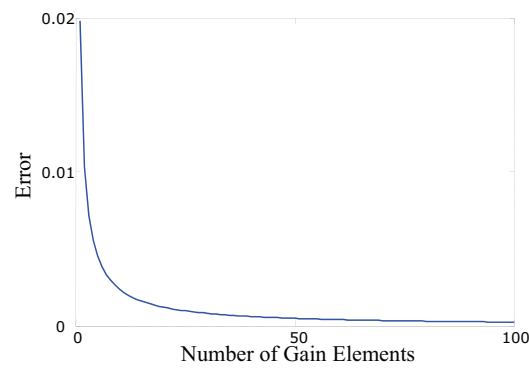


Figure 2.10: Modes of parallel waveguide cavities in weak coupling regime. The blue curves are results of the approximate solution and the red curves are the numerically calculated eigenvectors.



(a)



(b)

Figure 2.11: Error of parallel waveguide cavities in weak coupling regime. (a) The error as a function of coupling coefficient ($N = 7$), and (b) the error as a function of number of gain elements ($\alpha = 0.1$).

matrices \mathbf{B} and \mathbf{R} , where their summation satisfies equation (15).

$$\mathbf{B} = \begin{pmatrix} 1 & 1 & 0 & & 0 \\ 1 & 0 & 1 & 0 & \\ 0 & 1 & 0 & 1 & 0 \\ & & & \ddots & \\ & & 0 & 1 & 0 & 1 \\ 0 & & 0 & 1 & 1 \end{pmatrix} \quad (2.37)$$

and

$$\mathbf{R} = \begin{pmatrix} 1 & 0 & 0 & & 0 \\ 0 & 0 & 0 & 0 & \\ 0 & 0 & 0 & 0 & 0 \\ & & & \ddots & \\ & & 0 & 0 & 0 & 0 \\ & & 0 & 0 & 0 & 0 \\ 0 & & & 0 & 0 & 1 \end{pmatrix} \quad (2.38)$$

Under the strong coupling regime ($\alpha \rightarrow 1$), matrix \mathbf{R} approaches the null matrix. Therefore, in the strong coupling regime, eigenvectors of \mathbf{B} approximately diagonalize the round trip matrix \mathbf{M} . The eigenvalues of matrix \mathbf{B} are

$$\mu_i = 2 \cos \left(\frac{\pi(i-1)}{N} \right) \quad (2.39)$$

The eigenvectors of \mathbf{B} are the columns of matrix \mathbf{V} in equation 2.40 .

$$V = [v_{ik}]; v_{ik} = g_k \sqrt{\frac{2}{N}} \cos \left(\frac{(i-1/2)(k-1)\pi}{N} \right); g_k = \begin{cases} 1 & j \neq 1 \\ 1/\sqrt{2} & j = 1 \end{cases} \quad (2.40)$$

Based on the argument in section 2.10a, matrix \mathbf{V} defines the eigenmatrix of the round trip matrix \mathbf{M} approximately. Equation 2.41 illustrates the eigenvalues of the round trip matrix \mathbf{M} .

$$\lambda_i = \frac{1 - \alpha^2}{1 + \alpha^2 - 2\alpha \cos(\pi \frac{i-1}{N})} \quad (2.41)$$

Since $\lim_{\alpha \rightarrow 1} \lambda_1 = \frac{1-\alpha^2}{(1-\alpha)^2}$ is of indeterminate form, we evaluate λ_1 via equation 2.42.

$$\lambda_1 = 1 + \frac{(N-1)\alpha^2}{1-\alpha^2} - \sum_2^N \lambda_i \quad (2.42)$$

This equation resulted from the fact that the trace of \mathbf{M} is equal to the summation of the eigenvalues. Equation 2.39 describes how the eigenvector transformation affects \mathbf{R} .

$$(V^T R V)_{ik} = \begin{cases} 0 & i + j \text{ is odd} \\ \frac{4\alpha}{(1-\alpha)(N+1)} \sin\left(\frac{\pi i}{N+1}\right) \sin\left(\frac{\pi k}{N+1}\right) & i + j \text{ is even} \end{cases} \quad (2.43)$$

Equation 2.43 confirms that for $\alpha \rightarrow 1$, the error becomes negligible in the strong coupling regime. Figure 2.12 compares the approximate eigenvalues and eigenvectors under the strong coupling condition with their numerically calculated counterparts.

The figures 2.13 a and b below show the error as a function of coupling coefficient (α) and number of elements (N), respectively. We evaluate the relative root mean square error over all the eigenvalues. The plots confirm that for large number of gain elements ($N \rightarrow \infty$) and large coupling coefficient ($\alpha \rightarrow 1$) the error is negligible.

2.7 Cavity Sensitivity to Random Path-length Variations

In order to compare the performance of various cavity architectures when subjected to random phase errors, it is convenient to calculate the average phase error power loss where the average is taken over all possible phase errors ranging from 0 to 2π . In this section we calculate the phase-error loss for beam-splitter and Dammann grating cavities.

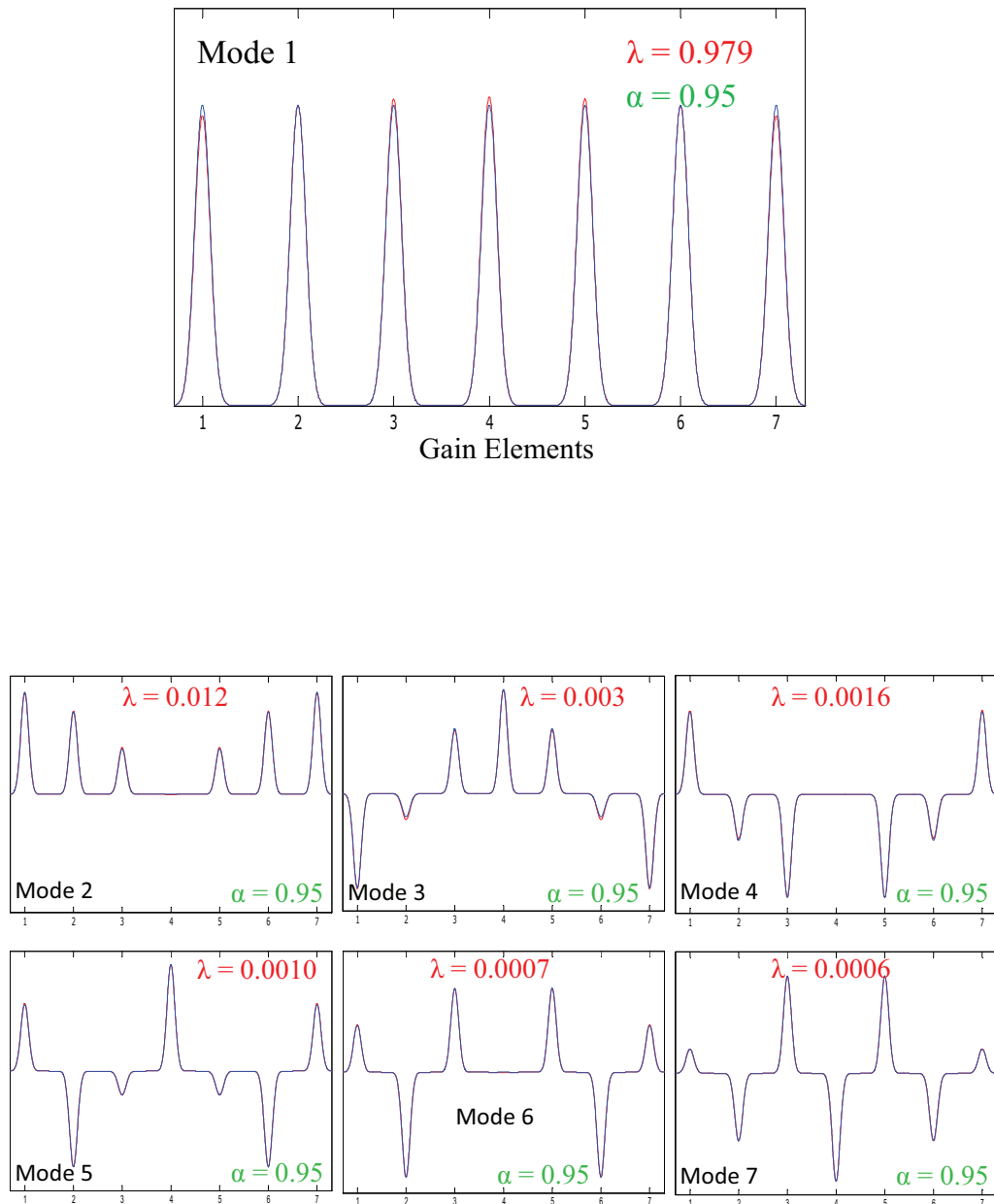
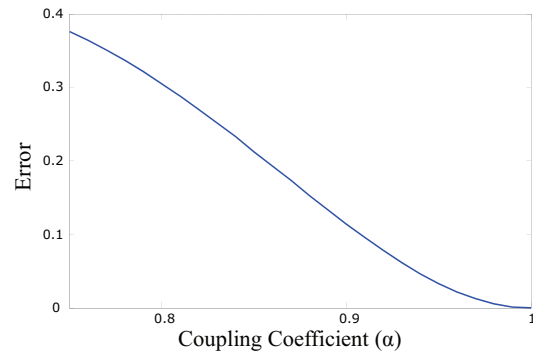
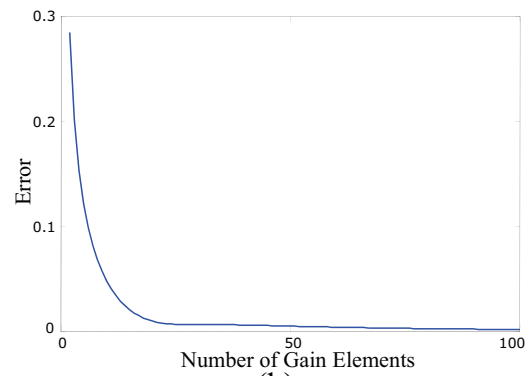


Figure 2.12: Modes of parallel waveguide cavities in strong coupling regime with $\alpha = 0.95$. The blue curves are results of the approximate solution and the red curves are the numerically calculated eigenvectors.



(a)



(b)

Figure 2.13: Error of parallel waveguide cavities in strong coupling regime. (a) The error as a function of coupling coefficient ($N = 7$), and (b) the error as a function of number of gain elements ($\alpha = 0.9$).

2.7.1 Beam-splitter Cavity

In the beam-splitter cavity, as is evident in eqs. 3.1 and 3.2, changes in path lengths ($\Delta\phi$) affect both the eigenvalue and the eigenvector. Since the eigenvector describes the fields in the two gain arms (a_1 and a_2), it is clear that a path length change, while inducing a phase shift between these two fields, does not change their respective intensities. This property of the mode is highly desirable, since power can be extracted most efficiently from both gain elements. On the other hand, the magnitude of the eigenvalue ranges from zero to r_o depending on the particular path length difference $\Delta\phi$. The phase of the eigenvalue simply indicates the operational wavelength of the laser. In general, the round-trip power loss to a particular resonator mode V_i is given by $1 - |\lambda_i|^2$. Therefore, for this single-mode cavity, the power loss is given by $1 - r_o^2 \sin^2(\Delta\phi/2)$. From this expression, we note that the loss consists of two parts. The first part contains the output coupler reflectivity, r_o^2 . This loss component can be chosen by the laser designer to maximize the power extracted from the cavity. The phase-dependent term, on the other hand, represents an undesirable loss (similar to the extra loss terms of scatter or diffraction in a conventional resonator). This additional loss component, which we term phase error power loss, generally reduces the power of the laser cavity and in some cases can suppress lasing altogether. Figure 2.14 shows the phase error power loss as a function of path length error, where the intensity reflectivity of the output mirror (r_o^2) has been set to unity. Thus, the curve represents additional undesirable loss introduced to the cavity as a result of path length errors.

In order to compare the performance of various cavity architectures when subjected to random phase errors, it is convenient to calculate the average phase error power loss where the average is taken over all possible phase errors ranging from 0 to 2π . Clearly, the average phase error power loss, obtained by integrating the cosine squared curve in fig. 2.14, is equal to 0.5. This result is expected since, by symmetry, a beam splitter must direct an equal amount of light to each port when all phases are represented.

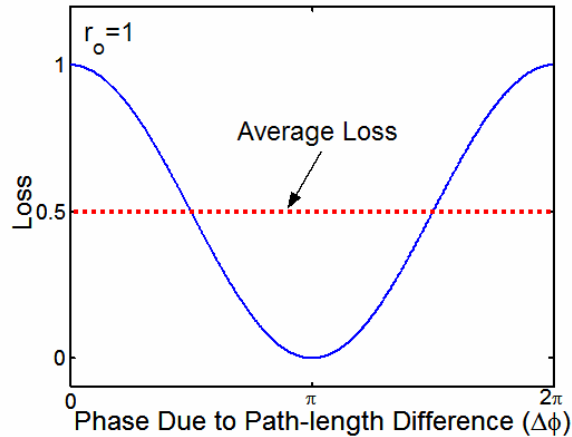


Figure 2.14: The loss as a function of path-length errors. The dotted line shows the average loss.

The same procedure confirms that the average phase-error-loss in extended Michelson cavities of figs. 2.2 is $1/4$. In general the average phase-error loss in a beam-splitter cavity containing N gain elements is $1/N$. Assuming each of the gain arms contribute same amount of power (P_0), in the presence of the phase-errors, the output power reduces to $NP_0 \times 1/N = P_0$. This could be interpreted as a manifestation of the radiance theorem.

2.7.2 Dammann Grating Cavity

The single-mode loss characterizing Dammann cavity in the presence of phase changes in one arm is shown in fig. 2.15. The contour plot in fig. 2.15(a) shows that there is only one phase state between elements that minimizes the loss (ideally to zero), whereas there are two states that maximize the loss (to unity). Plot 2.15(b) shows the effect of varying the phase in arm 3 when arm 1 and arm 2 are both set to $\pi/3$ radians, whereas plot 2.15(c) shows this effect when arm 1 is set to π and arm 2 is set to $\pi/3$ radians. The solid curves in fig. 2.15 (b) and fig.

2.15 (c) show the loss resulting from a real Dammann grating (designed by the optimization procedures of [23]), whereas the dashed curves show the loss from an ideal six-port device. This loss behavior can be generalized to any superposition element (such as an N-beam Dammann grating), and can be viewed as a manifestation of the radiance theorem; that is, if the phase states of N beams entering a single-mode superposition device are totally random, the average loss to this mode is such that no increase in radiance is possible.

The loss averaged across all possible phase errors is given by:

$$L = \frac{1}{(2\pi)^2} \int_0^{2\pi} \int_0^{2\pi} \left\{ 1 - \frac{r_o^2}{9} \left[3 + 2 \cos(\Delta\phi_1 - \frac{2\pi}{3}) + 2 \cos(\Delta\phi_3 - \frac{2\pi}{3}) + 2 \cos(\Delta\phi_1 - \Delta\phi_3) \right]^2 \right\} d(\Delta\phi_1) d(\Delta\phi_3). \quad (2.44)$$

Evaluating this integral shows that the average loss is given by $1 - r_o^2/3$. Separating the loss as before into output coupling loss and phase error power loss, it is clear that the phase error power loss is equal to $2/3$. This result is required by the symmetry of the six-port coupler, where each of the three output ports receives an equal amount of power under totally random phase conditions.

2.8 Conclusion

This chapter provides modal analysis for several common cavity structures. The modes and eigenvalues are deduced from the round-trip equation of the cavity. In forming the round-trip equation, the cavity elements are simulated based on geometric or wave optics approximations. Some the cavities including the Michelson cavity, Dammann grating cavity, volume Bragg grating cavity, and self-Fourier cavity support a single spatial supermode. The rest including Talbot cavity and parallel waveguide cavity are generally multimode, but can be under some specific conditions become single mode.

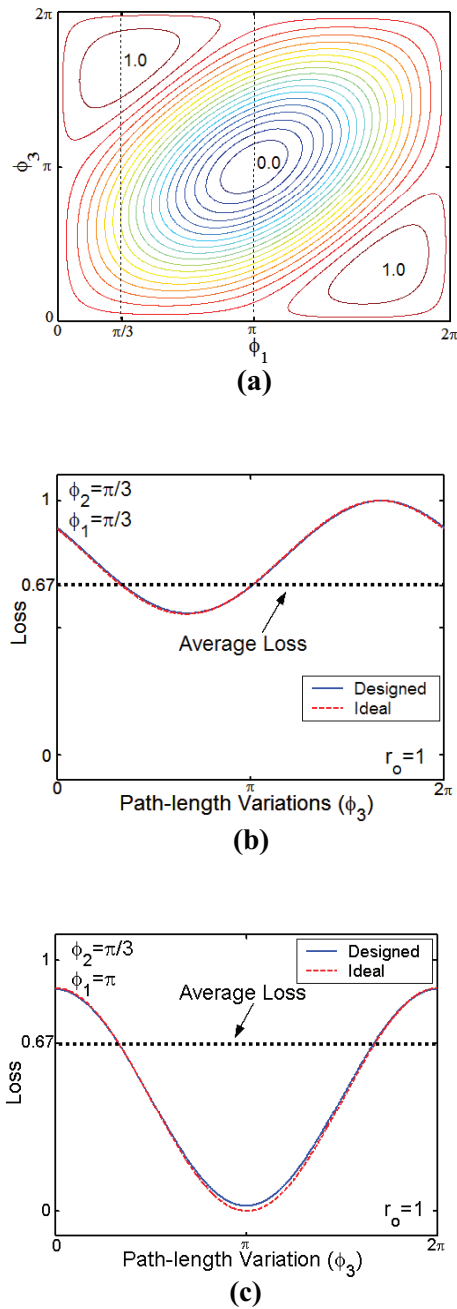


Figure 2.15: Effect of phase errors on the modal loss of a six-port Dammann grating. (a) Modal loss caused by phase errors in input arm 1 (ϕ_1) and input arm 3 (ϕ_3) for $\phi_2 = \pi/3$. (b) Modal loss as a function of phase error in input arm 3, where both ϕ_1 and ϕ_2 have a value of $\pi/3$ radians. Note that the difference between the designed and ideal curves is too small to see on this figure. (c) Modal loss as a function of phase error in input arm 3, where $\phi_1 = \pi$ and $\phi_2 = \pi/3$ radians.

In addition, a phase sensitivity analysis performed on Michelson cavity and Dammann grating cavity revealed that both these cavities are extremely sensitive to random path-length variations.

Chapter 3

Modal-Based Path-Length Sensitivity Reduction Techniques: Theory

In the previous chapter, as we described the modal response of several common cavities, it became clear that establishing coherence between the gain elements, though necessary, is not sufficient to improve the radiance. For example, it is shown with detail that in the standard Michelson cavity, the random path-length variations of the gain elements lower the output radiance to that of a single gain element laser. In this chapter we explain how and under what conditions the supermodes of the Michelson-type cavities, both spatial and longitudinal, can be exploited properly to reduce the sensitivity to path-length variations.

This chapter is organized as follows. Section 3.1 briefly reviews the modal response of the standard Michelson cavity. Section 3.2 introduces the generalized Michelson cavity and studies its modal behavior. Section 3.3 shows how the proper exploitation of spatial supermodes in the generalized Michelson cavity reduces the sensitivity to the random path-length variations. Section 3.4 explains under what conditions the longitudinal modes can help to reduce the sensitivity to the path-length variations. Finally, section 3.5 concludes this chapter.

3.1 Modal Analysis: Standard Michelson Cavity

As described in the previous chapter, the standard Michelson cavity (fig. ??) supports only one supermode

$$V = \begin{pmatrix} \frac{1}{\sqrt{2}} \\ \frac{j}{\sqrt{2}} e^{j\frac{\Delta\phi}{2}} \end{pmatrix}, \quad (3.1)$$

with an eigenvalue equal to

$$\lambda = -jr_o e^{j\frac{(\phi_2 + \phi_1)}{2}} \sin\left(\frac{\Delta\phi}{2}\right), \text{ where } \Delta\phi = \phi_2 - \phi_1. \quad (3.2)$$

Section 2.7 confirms that the standard Michelson cavity is sensitive to random path-length variations. When all phases (0 to 2π) are presented, the cold cavity analysis predicts that the output power does not exceed that of laser with single gain element.

Undefined in our analysis is the nominal operating wavelength of the collective lasing system. In a regular Fabry-Perot laser cavity the allowed operating wavelengths, also called the longitudinal modes, satisfy the self-consistency condition, which means the circulating electric field undergoes a total phase shift of an integral multiple of 2π . The laser, as a result, exclusively operates at wavelengths that creates real and positive eigenvalues. This same criterion is applied to the Michelson cavity to find the allowed longitudinal modes of the collective lasing system. Section 3.4 discusses the longitudinal modes of the common laser cavity.

3.2 Modal Analysis: Generalized Michelson Cavity

In the previous section, we showed that a standard Michelson resonator only supports one spatial supermode. This is a desirable feature, as it ensures that only one coherent state exists in the resonator. However, the price paid for this high modal discrimination (where modal discrimination is defined as $|\lambda_i|^2/|\lambda_j|^2$,

and λ_i is the eigenvalue of the i^{th} supermode) is a correspondingly high sensitivity to phase errors. We now explore the effect of replacing the beam block with a mirror of specified reflectance. We call this additional mirror the recycling mirror, as it attempts to recover a portion of the power that would otherwise be lost and injects this power back into the cavity. Our goal is to determine the effects of this recycling mirror on the cavity's modal structure as a function of path length phase errors.

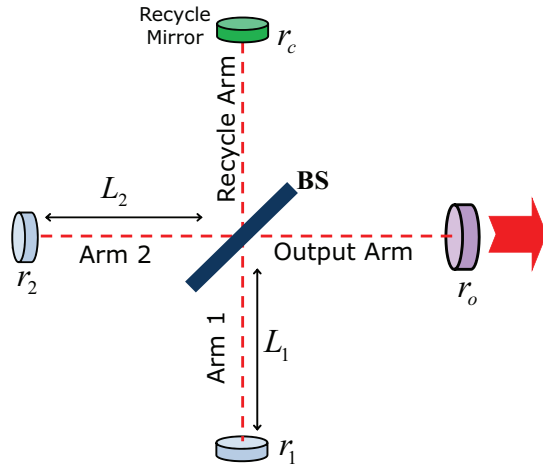


Figure 3.1: Beam-splitter resonator with mirrors in all arms. r_o : amplitude reflectivity of output mirror; r_r : amplitude reflectivity of recycle mirror.

Figure 3.1 shows the beam-splitter resonator with the recycling mirror in the arm labeled “Recycle Arm”. A similar approach as the one adopted in the previous section is followed to construct the round-trip matrix M_{rt} as:

$$M_{rt} = \begin{pmatrix} \frac{1}{2}(r_o - r_r)e^{j\phi_1} & \frac{j}{2}(r_o + r_r)e^{j\frac{(\phi_1 + \phi_2)}{2}} \\ \frac{j}{2}(r_o + r_r)e^{j\frac{(\phi_1 + \phi_2)}{2}} & \frac{1}{2}(r_r - r_o)e^{j\phi_2} \end{pmatrix} \quad (3.3)$$

In writing this matrix we have assumed that the optical path length of the output and recycling arms are precisely equal. The more general case, where these two path lengths are allowed to vary, is addressed in a subsequent section.

The eigenvectors and eigenvalues of this resonator are given by:

$$V1 = \begin{pmatrix} v_{11} \\ v_{21} \end{pmatrix}, V2 = \begin{pmatrix} v_{12} \\ v_{22} \end{pmatrix}$$

$$v_{11} = v_{12} = \frac{1}{\sqrt{2}}$$

$$\left. \begin{matrix} v_{21} \\ v_{22} \end{matrix} \right\} = \frac{j}{\sqrt{2}(r_o + r_r)} \left[(r_o - r_r)e^{-j\frac{\Delta\phi}{2}} + j(r_o - r_r) \right.$$

$$\left. \sin\left(\frac{\Delta\phi}{2}\right) \pm j\sqrt{(r_o - r_r)^2 \sin^2\left(\frac{\Delta\phi}{2}\right) + 4r_o r_r} \right]$$
(3.4)

and

$$\left. \begin{matrix} \lambda_1 \\ \lambda_2 \end{matrix} \right\} = \frac{-j}{2} e^{j\frac{\phi_1 + \phi_2}{2}} \left\{ (r_o - r_r) \sin\left(\frac{\Delta\phi}{2}\right) \right.$$

$$\left. \pm \sqrt{(r_o - r_r)^2 \sin^2\left(\frac{\Delta\phi}{2}\right) + 4r_o r_r} \right\},$$
(3.5)

where the upper (lower) values correspond to the positive (negative) roots of the two equations. Clearly, the addition of the recycling mirror has the potential to introduce an additional supermode. Since $v_{11} = v_{12} = 1/\sqrt{2}$, it must be the case that $|v_{21}| = |v_{22}| = 1/\sqrt{2}$, and it is only the phase angle between these two components that varies as a function of path length phase error. This implies that the intensities in both gain arms (arms 1 and 2 of fig. 3.1) are equal, independent of path length phase error. The round-trip loss suffered by each of these supermodes (corresponding to $1 - |\lambda_i|^2$) is shown in fig. 3.2 as a function of path length error for various values of recycling mirror reflectivity. Fig 3.2(a) indicates that, as the reflectivity of the recycling mirror (r_r) is increased, the loss to the first mode is less

affected by path length errors. On the other hand, increasing r_r also allows for a second supermode as seen in fig. 3.2(b), and the resultant modal discrimination of the cavity is reduced. It is this ability to trade off modal discrimination with path length sensitivity that allows one to tailor the cavity performance for maximum phase error tolerance.

3.3 Radiance Improvement Using Spatial Supermodes

We showed above that the intensity of the light circulating in each of the two gain arms (arm 1 and arm 2) of a four-port Michelson cavity was equal and independent of path length phase errors between the gain arms and mode number. However, the intensities in the output and recycle arms are very much dependent on these same path length phase errors and can be different for each mode. One obvious example of this is exhibited by phasing the gain arms to direct all the power into the output arm. The circulating power in each gain arm is still identical, but the output arm contains twice this value and the recycling arm contains no power. We now calculate the average power in the output arm of the four-port Michelson cavity when the path lengths of the gain arms are totally random and the average is performed across all possible phase states. If both modes are allowed to lase inside the cavity, we find that the total power in the output arm (and hence the radiance in this arm) does not increase over the power in a single gain arm. However, if the cavity has sufficient modal discrimination to suppress lasing of all but one mode, the power in the output arm can indeed be increased considerably even though the optical path length errors introduced by the two gain arms are assumed to be totally random. This occurs because the cavity modes and their corresponding eigenvalues change as a function of path length error, and under proper conditions the intensity distribution of the mode with the highest eigenvalue can strongly favor the output arm of the cavity. We have calculated

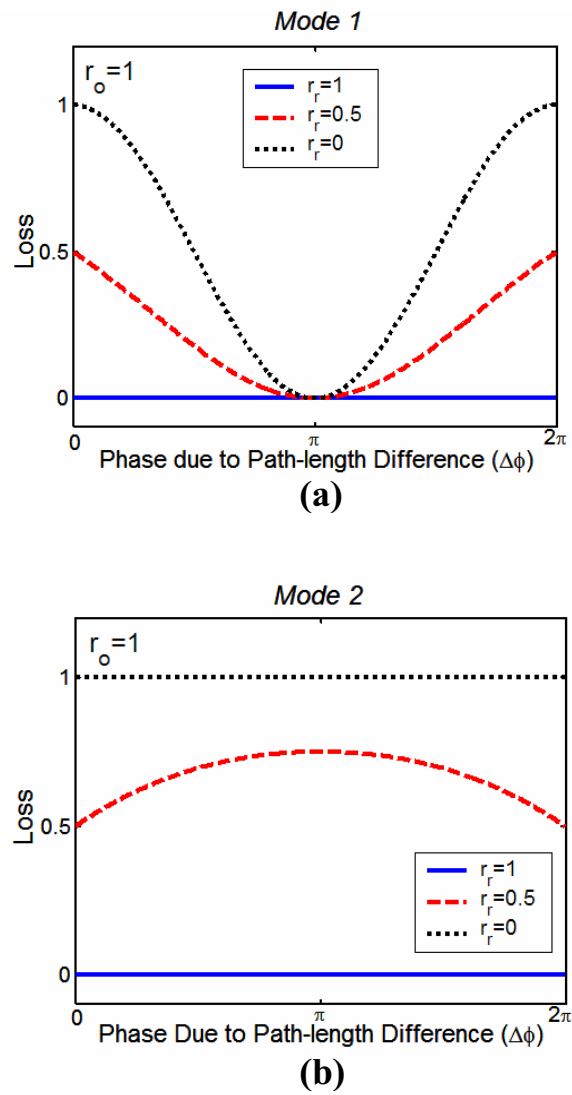


Figure 3.2: Losses associated with (a) mode one and (b) mode two of a Michelson cavity with three different recycling mirrors.

the average power present in the output arm as a function of the recycling mirror reflectivity (where the average is taken across phase errors from 0 to 2π) under the condition that the cavity only supports the lowest-loss supermode. If we define \overline{P}'_o , \overline{P}'_r , and \overline{P}'_g as the average circulating power in the output arm, recycle arm, and one of the gain arms respectively, the ratio of the power in the output arm to the power in one of the gain arms and the power in the recycle arm to the power in one of the gain arms are given by

$$\frac{\overline{P}'_o}{\overline{P}'_g} = \begin{cases} 1 - \frac{1}{2} \frac{|r_o - r_r|}{r_o + r_r} + \frac{1}{2\pi(r_o + r_r)} \left(4\sqrt{r_o r_r} + \frac{16r_o r_r + 4(r_o - r_r)^2}{2|r_o - r_r|} \right) \arcsin \frac{2|r_o - r_r|}{\sqrt{16r_o r_r + 4(r_o - r_r)^2}} & r_o > r_r \\ 1 & r_o = r_r \\ 1 + \frac{1}{2} \frac{|r_o - r_r|}{r_o + r_r} - \frac{1}{2\pi(r_o + r_r)} \left(4\sqrt{r_o r_r} + \frac{16r_o r_r + 4(r_o - r_r)^2}{2|r_o - r_r|} \right) \arcsin \frac{2|r_o - r_r|}{\sqrt{16r_o r_r + 4(r_o - r_r)^2}} & r_o < r_r \end{cases} \quad (3.6)$$

$$\frac{\overline{P}'_r}{\overline{P}'_g} = \begin{cases} 1 + \frac{1}{2} \frac{|r_o - r_r|}{r_o + r_r} - \frac{1}{2\pi(r_o + r_r)} \left(4\sqrt{r_o r_r} + \frac{16r_o r_r + 4(r_o - r_r)^2}{2|r_o - r_r|} \right) \arcsin \frac{2|r_o - r_r|}{\sqrt{16r_o r_r + 4(r_o - r_r)^2}} & r_o > r_r \\ 1 & r_o = r_r \\ 1 - \frac{1}{2} \frac{|r_o - r_r|}{r_o + r_r} + \frac{1}{2\pi(r_o + r_r)} \left(4\sqrt{r_o r_r} + \frac{16r_o r_r + 4(r_o - r_r)^2}{2|r_o - r_r|} \right) \arcsin \frac{2|r_o - r_r|}{\sqrt{16r_o r_r + 4(r_o - r_r)^2}} & r_o < r_r \end{cases} \quad (3.7)$$

These expressions are obtained by using the eigenmode of eq. 3.4 corresponding to the larger eigenvalue, propagating this field to the output arm, and calculating the resulting power in the output arm and recycle arm for a given path length phase error. This result is then integrated across all gain-arm phase errors

to obtain the average value.

Equation 3.7 suggests that the average output power is highly dependent on the ratio of reflectivities in the output and recycle arms. Figure 3.3 shows a graph of eq. 3.7, where the average circulating power in the output arm is plotted as a function of the recycle mirror reflectivity. Note that when the reflectivity of the output mirror is greater than the reflectivity of the recycle mirror, the power in the output arm can be substantially higher than that of the recycle arm. The maximum output arm power is achieved when the two mirror reflectivities are as close as possible, while still requiring $r_o > r_r$. When the reflectivity of the recycle arm surpasses that of the output arm, more power is directed towards the recycle arm. This behavior could be anticipated by simple symmetry considerations.

Equation 3.7 also suggests that when the two reflectivities become exactly equal, the system is no longer single mode and the average power drops to that of a single-gain-module. In this region, the modal discrimination becomes vanishingly small. Of course in practice, the cavity's ability to suppress higher-order mode oscillations is dependent on a number of factors, including modal gain competition and technical noise [19]. To achieve the maximum average output power in a realistic cavity, the value of r_r must be chosen to maximize \overline{P}_o while still preserving enough modal discrimination to ensure single supermode performance.

In our analysis we have assumed that the path lengths of the output and recycle arms are equal. These arms contain no gain elements and their path lengths can be arbitrarily short. As a result, precise control of this path-length difference is not as demanding as it is for the gain arms, and the desired phase relationship may conceivably be established by conventional opto-mechanical components. Nevertheless, it is important to explore the effect of output-recycle arm path length errors on overall average power. A laser cavity that deviates from the equal path length condition produces lower average circulating power in its output arm. Figure 3.4 shows the variations of the average circulating power (where, as before, the average is taken over all possible phase errors between the two gain arms) as a function of path-length difference between output and recycle arms. In this

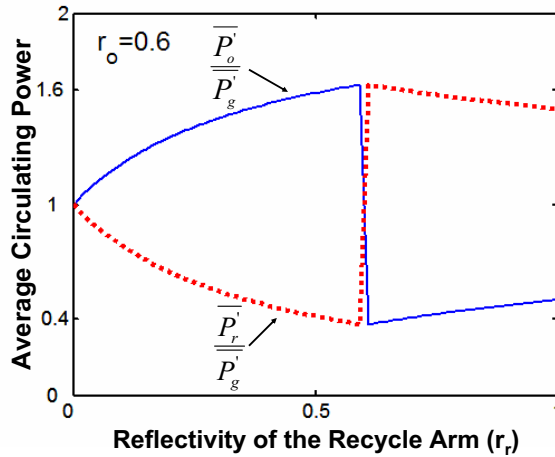


Figure 3.3: Power in the output arm (\overline{P}_o) and recycle arm (\overline{P}_r) as a function of recycle mirror reflectivity r_r . The prime quantities indicate circulating power.

simulation the reflectivity of the output mirror is assumed to be slightly greater than that of the recycle mirror. Figure 3.4 shows that phase deviations between the output and recycle arms can potentially reduce the average circulating power in the output arm. In the worst case, when the phase error is exactly π , the output arm contains an average power that is identical to the power in a single gain arm. If we now calculate the average across all possible phase errors in the output-recycle arms along with the average across all phase errors in the gain arms (i.e. no path length control over any of the four arms), this laser cavity delivers 74% of the power generated in the gain arms to the output arm. It should also be noted that, with output-recycle arms of differing path lengths, the two cavity eigenmodes no longer have equal intensities in the two gain arms, making the gain competition more complex and increasing the difficulty of achieving single supermode operation.

The power analysis presented here has concentrated on the circulating power inside the laser cavity. In practice however, the power coupled out of the cavity is of primary interest. To find the optimum output mirror reflectivity that maximizes

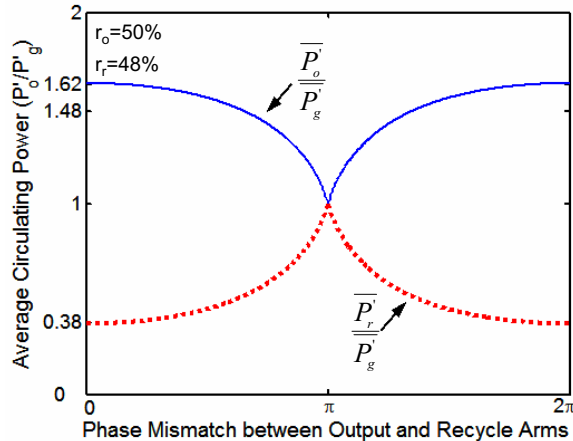


Figure 3.4: Average power in the output arm ($\overline{P'_o}$) and recycle arm ($\overline{P'_r}$) as a function of path-length difference between the output and recycle arms with $r_o = 50\%$ and $r_r = 48\%$. The prime quantities indicate circulating power.

the laser power outside the cavity, we apply the same strategy as developed in [25]. There are two loss mechanisms considered in that analysis. The output coupler represents a loss that contributes positively to the laser power. In addition, however, undesirable losses are present in the cavity, including diffraction, scattering, and unwanted reflection losses. The analysis finds the balance between the circulating power inside the resonator (which extracts stimulated emission from the gain medium) and output power, such that the total power produced by the laser is maximized.

The main difference between the above analysis for standard fabry-Perot laser cavities and the Michelson-type cavities described in this chapter is that here we include the phase error power loss from the coherent combining structure as an additional undesirable loss term. For a particular path length phase error in the gain arms, the dominant eigenvector is determined by choosing the largest eigenvalue using eq. 3.5. Equation 3.4 is then used to calculate a particular distribution of intensities in the output and recycle arms. The overall power attenuation of

this mode is calculated by multiplying this intensity distribution by the square of the dominant eigenvalue, and including all the additional unavoidable loss terms (diffraction, scattering, etc.) The output power of the cavity is then determined by observing the light distribution from the specific supermode and calculating the power transmitted by the output mirror. The power is then averaged over all possible path length phase errors in the gain arms. Finally, the output mirror reflectivity is optimized to maximize this average output power.

In a simple Fabry-Prot cavity the small signal gain as well as the internal losses dictate the optimum output mirror reflectivity to extract the highest possible power out of the cavity. In Michelson-type cavities, in addition to internal losses, the phase-error loss also affects the output power. As shown in fig. 3.2 (a) the phase-error loss reduces as the difference between the recycle and output reflectivities decreases. Of course, based on the sign of this difference more power may direct toward the recycle or output port. Figure 3.5 shows the result of a computer simulation using recycle mirror reflectivities between 0.15 to 0.90. We used a small signal gain of 30 dB and internal loss of -0.86 dB. In this simulation the reflectivity of the output mirror is optimized to extract the maximum power from either of the recycle port or the output port. For the cavity with these parameters, the maximum output power is achieved when the recycle mirror reflectivity is 0.59. Our simulation confirms that at this point the optimum output coupler has a slightly higher reflectivity of 0.60. In a real laser some reflectivity difference must be provided to ensure single-mode operation. Since our simulation did not consider modal gain competition effects, the marginal increase in reflectivity of the output mirror over the recycle mirror (0.01 difference) is resulted from the quantization in our simulation. For recycle mirrors with reflectivities lower than 0.59, the optimum output mirror reflectivity is slightly greater than the recycle mirror reflectivity and consequently more power is extracted from the output port. Conversely, for recycle mirrors with reflectivities higher than 0.59, the reflectivity of the output mirror is slightly lower than the recycle mirror and as a result more power is extracted from the recycle arm.

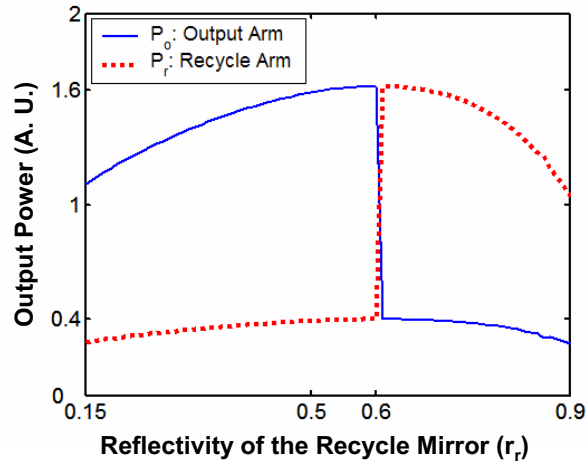


Figure 3.5: Laser output power as a function of recycle mirror reflectivity. The curve corresponds to a small signal gain of 30 dB, and additional unwanted losses of -0.86 dB.

3.4 Radiance Improvement Using Longitudinal Modes

So far in our analysis, the nominal lengths of the gain elements are assumed to differ slightly (due to the random path-length variations). Looking back at eq. 3.2, this causes all the longitudinal modes, corresponding to wave-numbers (k 's) that generate real and positive eigenvalues (eq. 3.2) and are in the gain-bandwidth of the laser, to become more or less equal. This assumption is valid as long as the path-length difference between the arms stays in the order of a few times the operational wavelength. For example, most semiconductor laser arrays consist of gain elements that are almost equal in length. However, in some lasing systems, most notably fibers, the nominal length difference can be quite large. This section studies the effect of the absolute value of the path-length difference on the output power of the standard Michelson cavity and finds a condition in which the longitudinal modes can be employed to reduce the sensitivity of the

output power to the path-length variations.

To better formulate the effect of the path-length difference (ΔL), we divide ΔL into two parts: a fixed part (ΔL_0), equal to the nominal length difference between the arms, and a small variable part corresponding to the random path-length variations (dl). The fix part is arbitrarily chosen and can be large, whereas, the random variations are at most a few times the nominal wavelength. In the same way, the gain bandwidth of the laser is assumed to span the nominal lasing wave-number k_0 by an amount $\pm\Delta k_{max}$. For example, the primary lasing line in Nd doped YAG at $\lambda = 1064$ nm ($k_0 = 5.9 \times 10^6$ m⁻¹) has the gain-bandwidth of 0.6 nm equivalent to $2\Delta k_{max} = 3300$ 1/m. It should be noted that the shape of the gain curve as a function of bandwidth is not uniform, and depending on the broadening mechanisms can be Lorentzian or Gaussian. The uniform shape assumed here is an approximation to the actual shape.

Considering the above definitions, the eigenvalue of the standard Michelson cavity is given by

$$\lambda = -jr_o e^{j(k_0 + \Delta k_i)(2L + \Delta L_0 + dl)} \sin((k_0 + \Delta k_i)(\Delta L_0 + dl)). \quad (3.8)$$

In this equation, $\Delta k_i = k_0 - k_i$ is in the range of $[k_0 - \Delta k_{max}, k_0 + \Delta k_{max}]$, where k_i 's are the wave-numbers that satisfy $Arg\{\lambda\} = 2\pi q$. The magnitude of the eigenvalue at these k_i 's is given by

$$|\lambda| = r_o |\sin(k_0 \Delta L_0 \pm \Delta k_i \Delta L_0 + k_0 dl \pm \Delta k_i dl)|. \quad (3.9)$$

In this equation, $\phi_0 = k_0 \Delta L_0$ is a constant. The term $\Delta k_i dl$ that is equal to $2\pi \frac{\Delta\lambda}{\lambda^2} dl$. For $dl < 10\lambda$, this term at most becomes equal to $20\pi \frac{\Delta\lambda}{\lambda}$. Since this term is quite small, it causes negligible phase shift that can be ignored. Applying this approximation, depending on the nominal length difference between the arms (ΔL_0), two regimes of operation can be identified.

- $\Delta k_{max} \Delta L_0 \ll 2\pi$: In this regime, the magnitude of the eigenvalue becomes

$|\sin(k_0 dl + \phi_0)|$. Since there is no Δk_i dependence, all possible longitudinal modes have virtually identical eigenvalues. In this regime, the modal analysis presented in 2.1 and 3.1 completely determines the response of this cavity. We refer to this regime of operation as the spatial-mode-dominant regime, since the output radiance of the cavity is forced by the spatial modes. As described in 3.1, no radiance improvement is observed in the standard Michelson cavity operating in this regime.

- $\Delta k_{max} \Delta L_0 \gg 2\pi$: In this regime, the magnitude of the eigenvalue becomes $|\sin(\pm \Delta k_i \Delta L_0 + k_0 \delta l + \phi_0)|$, which depends both on the wave-number and the path-length error. Particularly, for a fixed path-length error (dl), depending on the wave-number (k_i), the eigenvalue may have different magnitudes. Figure 3.6 shows the eigenvalues of the cavity with large path-length difference between the gain arms, as a function of the wave-number. The vertical lines are the possible longitudinal modes determined by the phase condition ($Arg\{\lambda\} = 2\pi q$). Assuming long enough cavities that support many longitudinal modes, the magnitude of the longitudinal modes can be any value between 0 and 1. It is also evident from the figure that the path-length error causes the pattern to move left and right, but the shape of the pattern remains unchanged.

In lasers with homogeneously broadened gain media, given enough discrimination between the longitudinal modes, the cavity exclusively supports the modes with the highest eigenvalues and suppresses the rest. As a result, given a Michelson cavity with enough path-length difference (large ΔL_0) and dense longitudinal mode content, the magnitude of the largest eigenvalue (or eigenvalues) remains in close proximity to 1, despite the random variations of the path-lengths. In fact, in response to path-length errors, the laser cavity hops from one longitudinal mode to another with the lowest loss. This, in turn, guarantees that the output radiance of this cavity is essentially insensitive to the random path-length variations. We refer to this regime of operation where the eigenvalue differs from one longitudinal

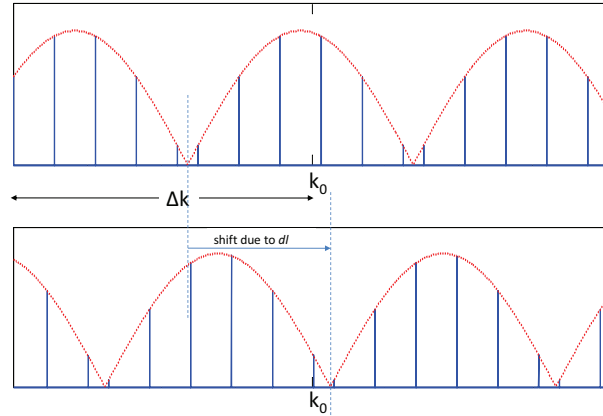


Figure 3.6: Longitudinal mode dominated regime. The solid vertical lines are the longitudinal modes, and the dotted curves are the gain curves.

mode to the next as the longitudinal-mode-dominant regime. Given a proper gain broadening mechanism, the standard Michelson cavity in the longitudinal-mode-dominated regime shows no sensitivity to path-length variations.

Figure 3.7 compares the output power of the standard Michelson cavity in spatial-mode-dominated and longitudinal-mode-dominated regimes. The longitudinal-mode-dominated cavity exhibits high output radiance and virtually no path-length error dependence.

What remains is the nominal path-length differences (ΔL_0 's) in between these two extreme regimes. For path-lengths in between, the average output power gradually increases from 0.5 to 1. Figure 3.8 shows the transition from spatial-mode dominated regime to longitudinal-mode-dominated regime. Here we assumed 1) infinite length of cavity (i.e. infinitely dense longitudinal modes), 2) flat gain curve ranging from $-\Delta k_{max}$ to $+\Delta k_{max}$, the gain-bandwidth assumed for Nd: in a YAG host ($2\Delta k_{max} = 3300$ 1/m).

Finally, the normalized output power averaged over all the possible path-length

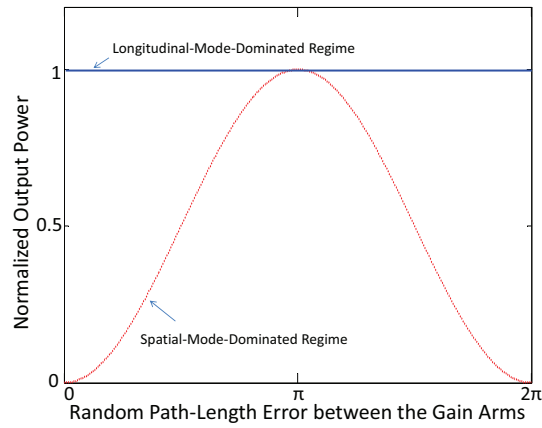


Figure 3.7: Comparison between the output power of the standard Michelson laser in the longitudinal-mode-dominated regime and spatial-mode-dominated regimes.

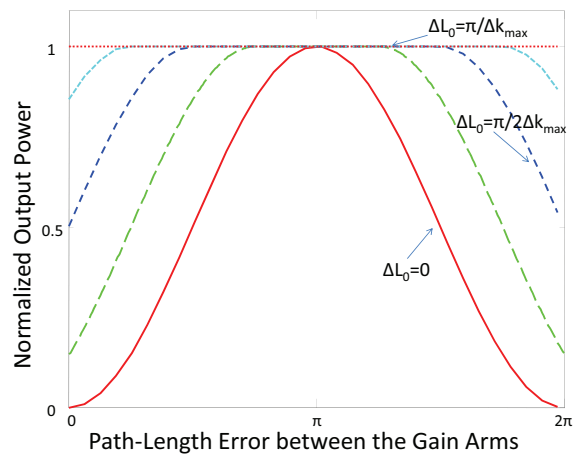


Figure 3.8: Gradual Transition from spatial to longitudinal mode dominated regime.

errors is shown in fig. 3.9 as a function of the nominal length difference between the gain arms.

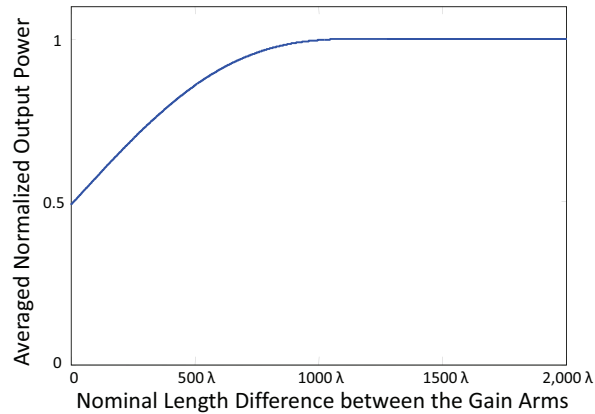


Figure 3.9: Gradual Transition of the normalized output power averaged over all the possible path-length errors.

3.5 Conclusion

This chapter systematically analyzed the modes of the generalized Michelson cavity. It was shown that totally blocking light from all output ports but one permits oscillation in only a single supermode. Under perfect phasing conditions, these structures were seen to perform perfect beam addition with the radiance of the output equal to the sum of the radiances from the individual sources. However, under totally random phasing conditions of the input arms, these same architectures did not increase the average radiance above that of a single source. If, however, these superposition structures were modified to return some of the previously blocked light back to the resonator, a second mode was introduced to the cavity. The discrimination between these modes was seen to be a function of both

path length errors and mirror reflectivities. Furthermore, a laser that could maintain oscillation in a single lowest-loss supermode showed substantial tolerance to path length errors. In general, the method appears to provide a design trade-off between mode discrimination and path length tolerance that could be useful in constructing practical coherent laser beam combining systems. Further, a systematic study showed the role of longitudinal modes in reducing the sensitivity to path-length variations in the standard Michelson cavity with large path-length difference between the gain arms.

Chapter 4

Modal-Based Path-Length Sensitivity Reduction Techniques: Experiment

This chapter complements the previous chapter by providing experimental support to the modal-based path-length sensitivity reduction techniques in Michelson-type cavities. When possible, the eigenmodes, eigenvalues, and output powers in spatial-mode-dominated and longitudinal-mode-dominated cavities are measured and compared with the modal analysis results. This comparison identifies the potential of the modal analysis to accurately predict the main characteristics of the cavity.

This chapter is organized as follows. Section 4.1 identifies the obstacles in performing meaningful measurements with the Michelson cavity and introduces the fully common-path polarization multiplexed cavity as an alternative. In the following sections, the modes, eigenvalues (or equivalently phase-error loss), and output powers of the standard Michelson cavity (section 4.2.1), generalized Michelson cavity (section 4.2.2), and standard Michelson cavity with large path-length difference between the gain arms (section 4.3) are measured and compared with the modal theory. Section 4.4 is reserved for concluding remarks.

4.1 Experimental Considerations

The experimental demonstration of the spatial supermodes in the generalized Michelson cavity of fig. 4.1 demands considerable precision. First, the path-lengths of the gain arms on one side and the output and recycle arms on the other side must be kept sufficiently close ($\Delta L \ll \frac{1}{\Delta K}$) to prevent longitudinal mode hopping effect described in 3.3. Second, to study the effect of a known path-length error, that error must be determined to better than a fraction of the operational wavelength. Third, in the Michelson cavity of fig. 4.1, it is very difficult to perform some measurements, for example, the relative phase shift between the components of the eigenmode.

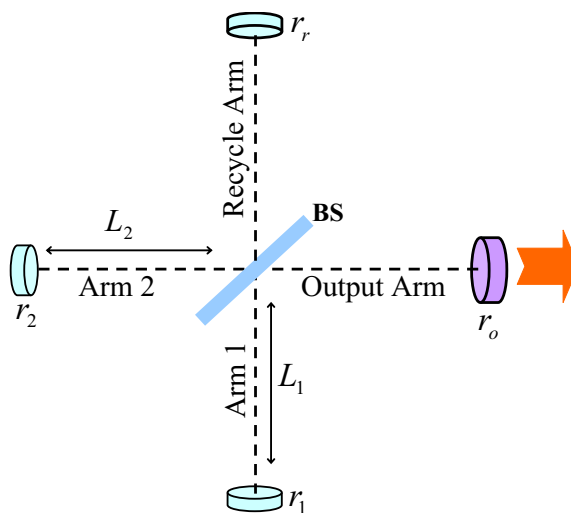


Figure 4.1: Generalized Michelson cavity. r_o : amplitude reflectivity of output mirror; r_r : amplitude reflectivity of recycle mirror.

Polarization multiplexing the beams of the gain arms and the beams in the output and recycle arms to form a common-path cavity solves these three problems at once. The lengths of the gain arms can be held equal (assuming no elements with birefringence), and also the lengths of the output and recycle arms can be kept exactly equal. These common paths considerably reduce the sensitivity of the

length difference (ΔL) to physical changes. This allows precise control of the path-length difference ($\Delta\phi$). Finally, the polarization multiplexed cavity facilitates the measurements of the relative amplitudes and phases through polarimetry because the two beams are already superimposed.

It should be noted that since the electric field is a vector, it is characterized by a two-dimensional space. This means that two completely independent degrees of freedom can be accessed. Placing the beams on top of one another should, in no way, be different from placing them in physically distinct locations. As long as there is no gain competition, this common cavity polarization-multiplexed system is exactly the same as the Michelson cavity.

The polarization multiplexed equivalent of the Michelson cavity must contain elements to 1) differentially change the path lengths of the two polarization states, 2) split and add two polarization states, and 3) reflect differing amounts of light in the two polarization states.

Figure 4.2 illustrates the polarization multiplexed equivalent of the generalized Michelson cavity of fig. 4.1. Here, the two orthogonal states of polarization, vertical and horizontal, represent the beams in the two gain arms. Similarly, on the output side of the cavity, vertical and horizontal polarizations represent the beams in the output and recycle arms, respectively. On the gain side, the combination of the two half-wave plates with fast and slow axes along the vertical and horizontal directions generates a phase shift between the gain arms. Tilting the first half-wave plate by θ degrees about the optical axis of the cavity creates $\Delta\phi = kd[(\sqrt{n_e^2 - \sin^2\theta} - \sqrt{n_o^2 - \sin^2\theta}) - (n_e - n_o)]$ phase shift between the two polarization states. Here, d is the thickness of each half-wave plate, k is the operational wave-number, and n_e and n_o are the extraordinary and ordinary refractive indices. It is clear that $\Delta\phi$ is essentially constant over the entire gain bandwidth of the laser. The split/add function is performed by the quarter-wave plate with fast axes rotated 45 degree to the horizontal. Finally, the cavity utilizes a tilted piece of glass or a polarizer and a mirror to generate differential reflectivity between the output and recycle beams. The two polarizations (vertical and horizontal) show

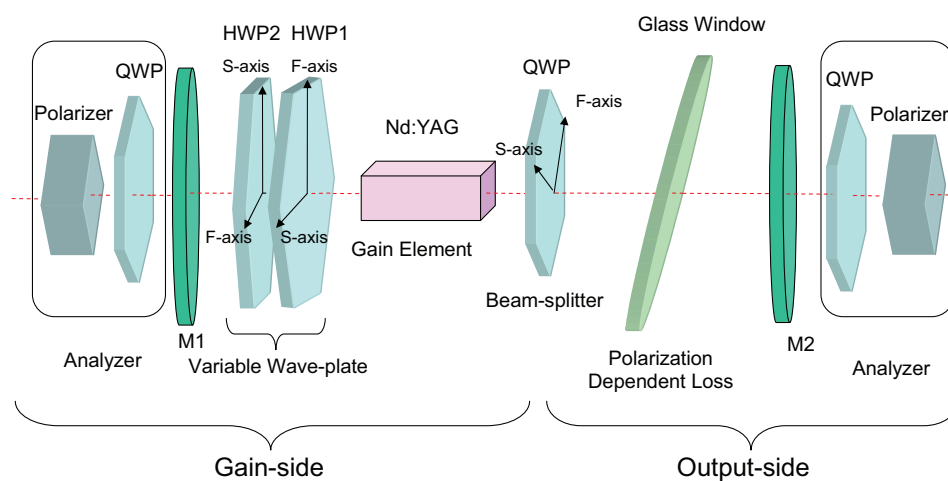


Figure 4.2: Experimental set-up of polarization multiplexed cavity. HWP: half-wave plate, QWP: quarter-wave plate, pol:polarizer, M1 and M2: mirrors

different transmittivities at oblique incidence at the air-glass interface. For the standard Michelson cavity with $r_r = 0$, a polarizer in the vertical direction directs all the horizontally polarized light out of the cavity and ensures zero reflection from recycle arm.

Our polarization multiplexed cavity is 40 cm long, with mirrors of $M1 = 99.9\%$, $ROC = 1.25$ m, and $M2 = 97.5\%$, $ROC = 0.75$ m on the gain side and output side, respectively. The gain element is a slab of $5\text{ mm} \times 5\text{ mm} \times 15\text{ mm}$, 1.1% Nd:YAG crystal. No birefringence is observed in the Nd:YAG crystal. The half-wave plates are multiple order (almost 1mm thick) and made out of quartz. The axes (fast and slow) of one are perpendicular to those of the other to balance the path-lengths. Both half-wave plates are anti-reflection coated at 1064 nm for normal incidence. The variable wave plate created by tilting one of the half-wave plates causes a negligible lateral separation on the order of a tenth of a micron between the two polarizations. We use a zero-order quarter-wave plate as the beam-splitter almost at the middle of the cavity. It is also AR-coated at 1064 nm for normal incidence. The differential reflectivity is provided by tilting a 5 mm thick, one-side AR-coated at 1064 nm BK7 glass window with refractive index of 1.56. The glass thickness is chosen to suppress Fabry-Perot resonances by creating relatively large walk-off angles for small tilts. In cases where the glass is replaced by a polarizer, a Glan Brewster-angle polarizer is used to minimize the reflection loss.

The modal analysis of the polarization multiplexed cavity further confirms the equivalence of the polarization multiplexed and Michelson cavities. It is easy to verify that the Jones matrices of the polarization cavity elements (tilted half-wave plate, quarter wave plate, and tilted glass) are identical to the scattering matrices of the corresponding elements of the Michelson cavity (Φ , S , R as defined in eq. 2.2). Since the round-trip equations of both cavities are identical, the polarization modes of the multiplexed cavity exactly match, both in form and in characteristics, the modes of the Michelson cavity.

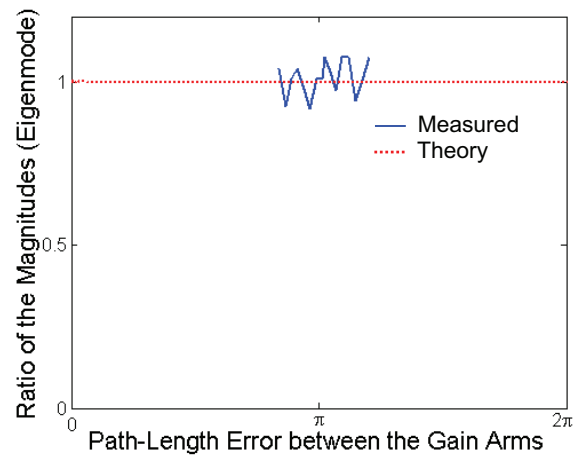
4.2 Spatial Supermodes

In this section, we first perform a number of experiments to study the modal response of the standard Michelson cavity in the presence of path-length error between the gain arms. Next, we investigate the effect of the recycle mirror on the modal response and output power.

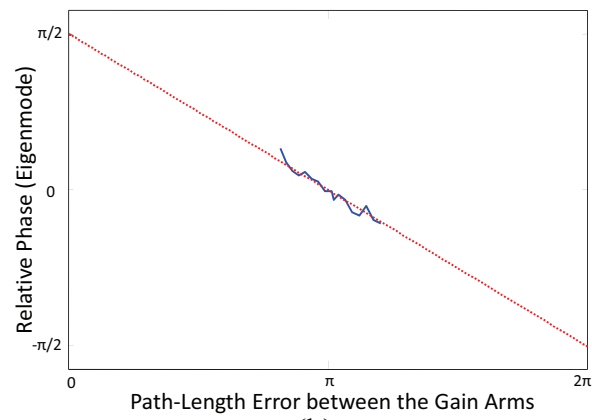
4.2.1 Standard Michelson Cavity ($r_r = 0$)

For the polarization multiplexed equivalent of the standard Michelson cavity the tilted glass in fig. 4.2 is replaced by a vertical polarizer. The polarizer generates a differential reflectivity between the output and recycle arms ($r_o = 0.99$, $r_r = 0$). On each side of the cavity the output beam is examined by a polarizer and a quarter-wave plate. In order to find the polarization state of the beam, the polarizer and quarter-wave plate are rotated until a null is created. The polarization state of the beam is then inferred from the two rotation angles. The resulting polarization state is then decomposed into a vertical and a horizontal component with a phase shift between them. Note that the formation of the null implies that the polarization multiplexed cavity operates in a single polarization mode. Because of the way we defined the eigenmodes in the previous section, we examine the output beam in the gain-side of the cavity. The magnitudes of the vertical and horizontal components and the phase shift between them determine the magnitude ratio and relative phase between the components of the eigenmode.

Figures 4.3 a and b compare the magnitude ratio and relative phase of the eigenmode components with the theoretical results of the modal analysis given in eq. 3.2. First of all, since the cavity remains below threshold for larger deviations from the ideal path-length condition (π phase shift), the theoretical hypothesis and the experimental results can only be partially compared. As seen in the figure, the limited experimental data available supports the modal analysis predictions. The magnitude ratio of the eigenmode components is nearly one for all the path-length errors. This means the two polarization channels (vertical and horizontal)



(a)



(b)

Figure 4.3: (a) Magnitude ratio and (b) relative phase of the components of the eigenmode for the cavity with $r_r = 0$.

have the same intensity independent of the path-length error. In the absence of the recycle mirror, the relative phase between the components of the eigenmode is proportional to the path-length error.

To suppress the effect of extraneous loss like the desirable loss of the output coupler, we measured the phase-error loss instead of the eigenvalue. To determine the phase-error loss we first measure the output power (power in the vertical polarization from the output side), for a given path-length error. Then we construct a calibration curve by adding known losses to the cavity with no phase-error loss (π phase-shift between the gain arms). The variable loss for calibration is provided by tilting a piece of glass. Finally, with the help of the calibration curve we find the phase-error loss corresponding to the measured output power. Fig. 4.5 compares the measured phase-error loss with the loss anticipated from the modal analysis. Again, the range of the phase error is limited due to the available gain, but the data appears to confirm the results of the modal analysis of previous chapter.

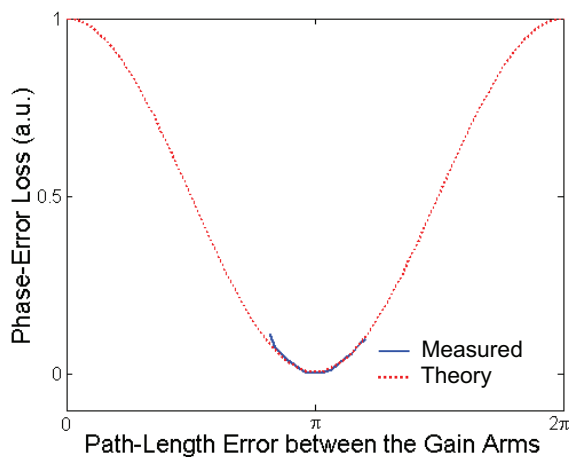


Figure 4.4: Phase error loss of the standard Michelson cavity with $r_o = 0.99$ and $r_r = 0$. The solid line is the experimentally measured phase-error loss, and the dotted line is the loss anticipated from modal analysis.

Finally, the normalized output power for different path-length errors is shown in fig. 4.5. The average normalized output power over all path-length errors (0 to 2π) is 0.0943. It should be noted that the laser gain is inherently nonlinear due to its threshold behavior. To calculate the output power, a prior knowledge of all the loss including the internal loss and output coupler loss, as well as the small signal gain is required. The dashed line in fig. 4.5 shows the output power dictated by the modal analysis (no nonlinear effect).

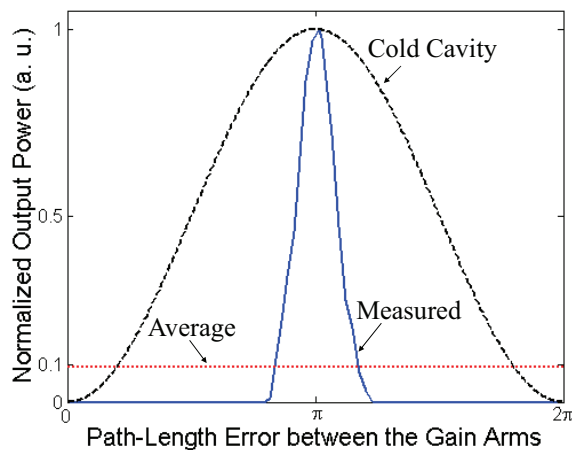


Figure 4.5: Output power of the generalized Michelson cavity with $r_r = 0.99$ and $r_o = 0$. The dotted line shows the average power over all path-length errors.

It should be noted that the theoretical output power is determined assuming the gain elements are linear and there is no other source of loss in the cavity besides the phase-error loss. In practice, the gain elements do not entirely operate in the linear regime (threshold and saturation are two examples of the nonlinear response of the gain elements). In addition, besides the phase-error loss, there are other sources of loss in the cavity, for example the reflection loss caused by non-optimal AR coating of the cavity elements and the useful output coupler loss. To calculate the precise theoretical output power, one must determine the small

signal gain and the cavity loss as described in the previous chapter.

4.2.2 Generalized Michelson Cavity ($r_r \neq 0$)

The tilted piece of glass in the setup of fig.4.2 results in a nonzero recycle mirror reflectivity ($r_r \neq 0$). Here, we examine the performance of the cavity at two points; one with a piece of uncoated glass adjusted at Brewster's angle ($r_r = 0.745, r_o = 0.999$), and one such that the vertical polarization experiences a slightly higher transmittivity (corresponding to $r_o = 0.96$ and $r_r = 0.94$). As explained in the theoretical section, the Michelson cavity with $r_r \neq 0$ supports two supermodes. However, since the two supermodes completely overlap spatially, gain competition suppresses one mode given sufficiently different eigenvalue magnitudes. In this section, whenever possible, the dominant eigenmode and its associated phase-error loss are experimentally measured.

Figures 4.6 a and b show the magnitude ratio and relative phase shift between the components of the dominant eigenmode for the cavity with $r_r = 0.745, r_o = 0.999$. Like the standard Michelson cavity, the magnitudes of the eigenmode components are equal, independent of the applied phase-error. The relative phase between the components, compared to the standard Michelson cavity, varies less. This is expected since the relative phase shift is no longer forced merely by the beam-splitter.

Figure 4.7 illustrates the phase-error loss associated with the dominant eigenmode. A comparison with the standard Michelson cavity ($r_r = 0$) in fig. 4.4 reveals that the dominant eigenmode of the generalized Michelson cavity with $r_r = 0.745$ experiences lower loss. Obviously, the reduced loss improves the output power. Figure 4.8 shows the output power generated by the generalized Michelson cavity with $r_o = 0.999$ and $r_r = 0.745$. The output power clearly benefited from the recycle mirror. The normalized output power averaged over all path-length errors is 0.23.

Now we replace the uncoated glass with a coated glass and change the tilt

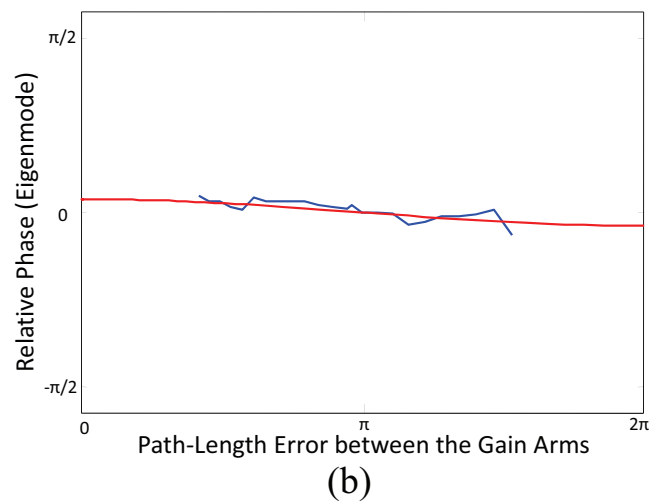
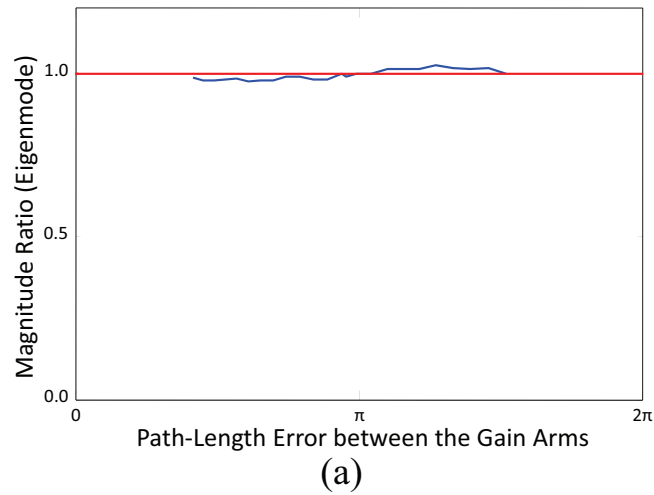


Figure 4.6: (a) Magnitude ratio and (b) relative phase shift between the components of the dominant eigenmode in the generalized Michelson cavity with $r_o = 0.999$ $r_r = 0.745$. The solid lines are the experimentally measured, and the dotted lines are the results anticipated from modal analysis.

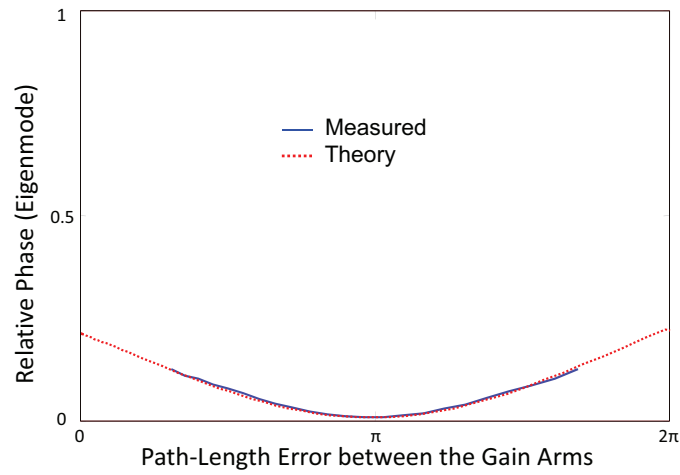


Figure 4.7: Phase-error loss associated with the dominant mode of the generalized Michelson cavity with $r_o = 0.999$ and $r_r = 0.745$. The solid line is the experimentally measured phase-error loss, and the dotted line is the loss anticipated from modal analysis.

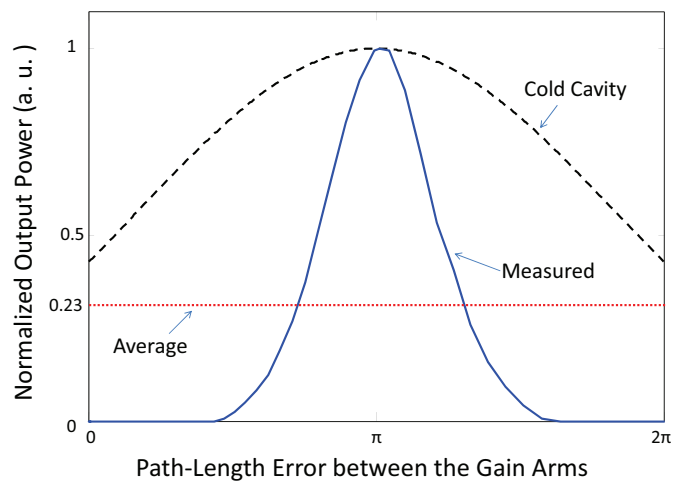
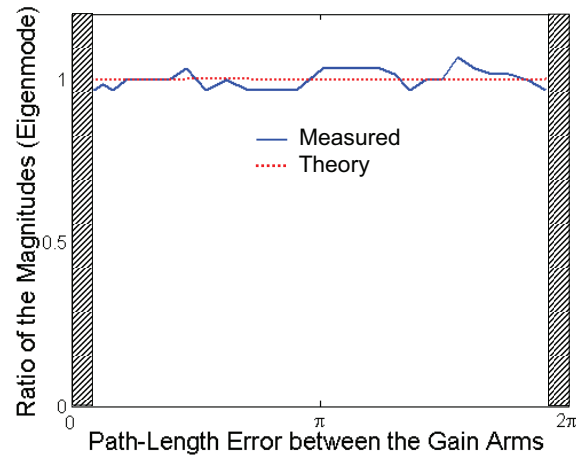


Figure 4.8: Output power of the generalized Michelson cavity with $r_r = 0.999$ and $r_o = 0.745$. The dotted line shows the average power over all path-length errors.

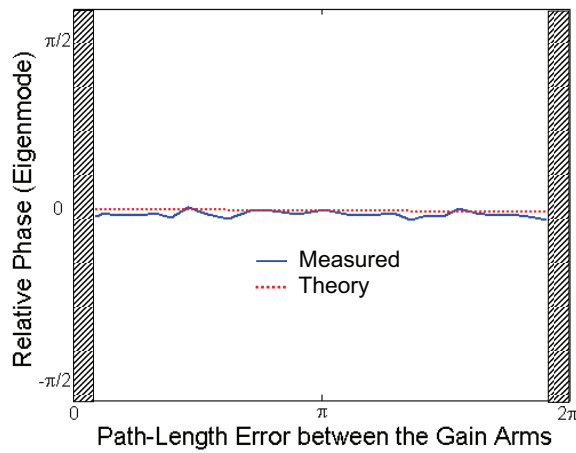
angle to create higher recycle mirror reflectivity. At this point, the measured reflectivities are $r_o = 0.96$ and $r_r = 0.94$.

Figures 4.9 a and b show the magnitude ratio and relative phase shift between the components of the dominant eigenmode. Again, the magnitudes of the eigenmode components are equal, independent of the applied phase-error, and the relative phase between the components varies even less. Here, the laser system remains above threshold for all path-length errors. Interestingly, at phase-errors close to 0 and 2π , the discrimination between the eigenvalues diminishes, and the two polarization modes start to operate simultaneously. The existence of two mutually incoherent polarization modes results in an unpolarized beam, which simply means that the combination of the polarizer and quarter-wave plate fails to generate a null. In fig. 4.9 the regions where both modes operate simultaneously are covered by hashed lines. Based on the modal analysis, in these regions the discrimination between the two modes almost vanishes.

Figure 4.10 illustrates the phase-error loss associated with the dominant eigenmode. A comparison with the standard Michelson cavity ($r_r = 0$) in fig. 4.4 and the cavity with $r_o = 0.999$, and $r_r = 0.745$ in fig. 4.7 reveals that the dominant eigenmode of the generalized Michelson cavity with $r_r = 0.94$ experiences a substantially lower loss. The lower phase-error loss is the reason that the laser system remains above threshold for all path-length errors, though the reflectivity of the output coupler (0.96) is lower in comparison to the other two cavities (0.99 and 0.999). Obviously, the reduced loss improves the output power even more. Figure 4.11 shows the output power generated by the generalized Michelson cavity with $r_o = 0.96$ and $r_r = 0.94$. The normalized output power averaged over all path-length errors is 0.67, slightly more than seven times the average output power of the standard Michelson cavity (0.0943). This seven-fold increase in the output power is an indication of the lower sensitivity of the output power to random path-length variations.



(a)



(b)

Figure 4.9: (a) Magnitude ratio and (b) relative phase shift between the components of the dominant eigenmode in the generalized Michelson cavity with $r_o = 0.96$ $r_r = 0.94$. The solid lines are the experimentally measured, and the dotted lines are the results anticipated from modal analysis.

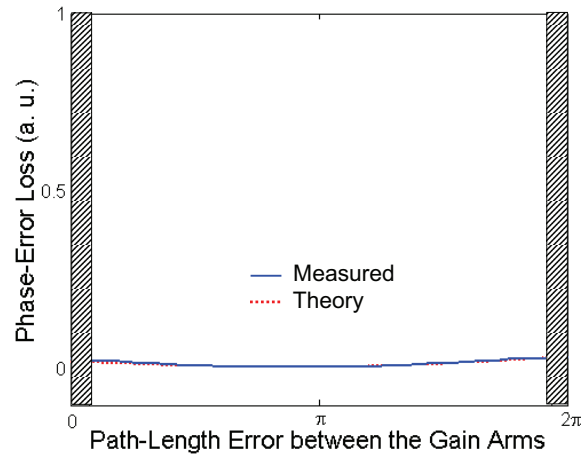


Figure 4.10: Phase-error loss associated with the dominant mode of the generalized Michelson cavity with $r_o = 0.96$ and $r_r = 0.94$. The solid line is the experimentally measured phase-error loss, and the dotted line is the loss anticipated from modal analysis.

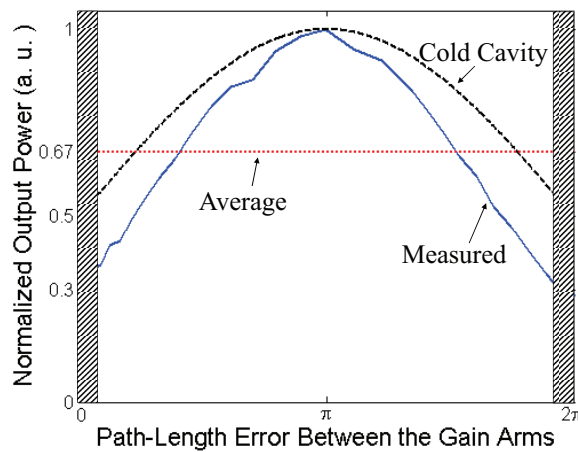


Figure 4.11: Output power of the generalized Michelson cavity with $r_r = 0.96$ and $r_o = 0.94$. The dotted line shows the average power over all path-length errors.

4.3 Longitudinal Modes

In the longitudinal-mode-dominated regime, the nominal path-length between the gain arms is rather large. To study the effect of path-length error on the output power in the longitudinal-mode dominated regime ($\Delta L \gg \frac{1}{\Delta k}$), in addition to the tilted half-wave plate an optical element is required to generate a large phase-shift between the two polarization states. In the set-up shown in fig. 4.12, this path-length difference is provided by a pair of calcite walk-off polarizers.

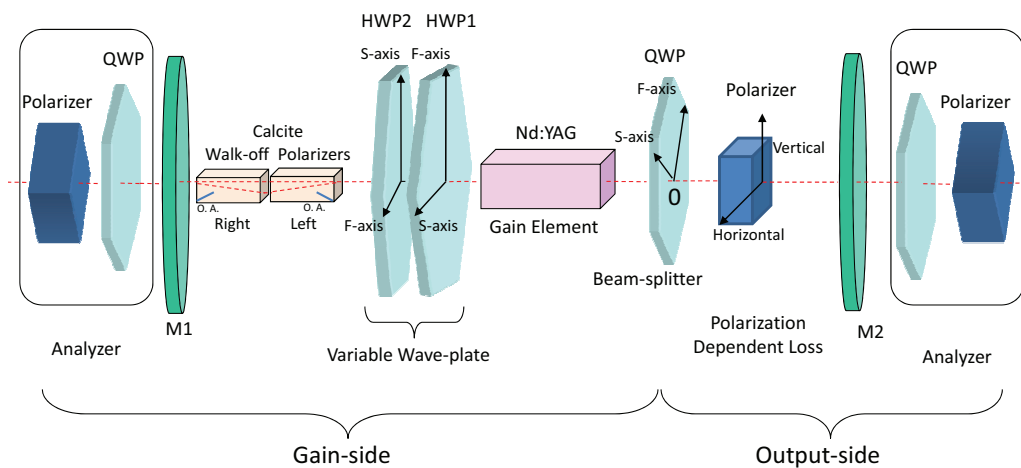


Figure 4.12: Set-up of the polarization multiplexed cavity with calcite walk-off polarizers.

The walk-off polarizer is a slab of calcite, cut such that the optical axis is oriented at 42° in respect to the x-axis. This results in the spatial separation of

the two polarization eigenmodes of the linear medium (vertically and horizontally polarized beams). Moreover, the two polarization states undergo different paths and acquire a phase shift proportional to the length of the walk-off polarizer. The phase shift is $\phi(L) = k_0 n_o L \left[\frac{n_e}{\sqrt{n_e^2 \cos^2(42^\circ) + n_o^2 \sin^2(42^\circ)}} - 1 \right]$, where k_0 is the nominal wave-number, n_o and n_e are the ordinary and extraordinary refractive indices of calcite (1.6584 and 1.4864 at $\lambda = 1064$ nm, respectively), L is the length of the walk-off polarizer, and 42° is the angle between the optical axis of the calcite crystal and the optical axis of the cavity. The effective path-length difference between the two polarization states is $\Delta L = \frac{\phi}{k_0 n_o}$. The walk-off polarizers used in this experiment are AR coated at 1064 nm to minimize the loss. Of course instead of walk-off polarizers, we could have used wave-plates to generate the desired phase-shift between the gain elements. For quartz wave-plates the required thickness is about 20 cm.

We placed the pieces of calcite walk-off polarizer with overall lengths of 8 mm and 20 mm, corresponding to $\Delta L_0 = 0.4$ mm and $\Delta L_0 = 1.0$ mm path-length difference in the gain side of the cavity as shown in fig. 4.12. Further, we tilted the half-wave plate, as usual, to create a 0-to- 2π round-trip phase error between the gain arms.

Figure 4.13 shows the output power as a function of the path-length error that is applied by the tilting half-wave plate for the nominal path-length difference (ΔL_0) of 0 mm (solid), 0.4 mm (dashed), and 1.0 mm (dotted).

It is clear from this figure that as the nominal path-length difference between the gain arms (ΔL_0) increases, the output power becomes less and less sensitive to random path-length variations. The averaged normalized output power for the cavities with $\Delta L_0 = 0$, $\Delta L_0 = 0.4$ mm and $\Delta L_0 = 1.0$ mm is 0.095, 0.337, and 0.665, respectively. The effect described in 3.4 explains this reduced sensitivity. In fact, if we consider the Michelson cavity as a combination of two separate cavities, each containing one of the gain elements, the large path-length difference between the gain arms increases the possibility of finding a common longitudinal mode.

It should be noted that the tilting half-wave plate introduces some loss due to

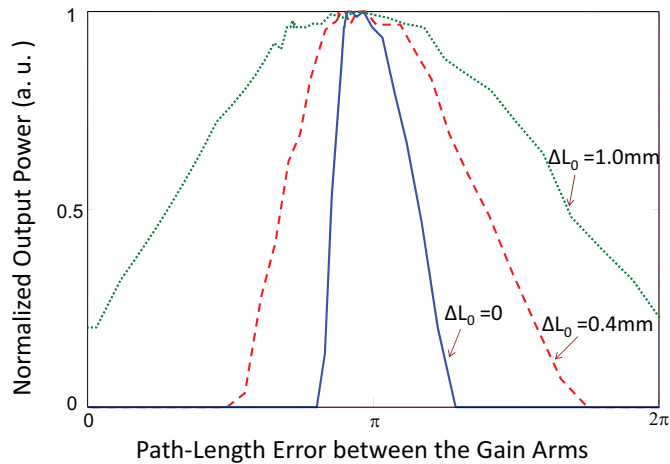


Figure 4.13: Output power for cavities with $\Delta L_0 = 0$ (solid), $\Delta L_0 = 0.4$ mm (dashed), $\Delta L_0 = 1.0$ mm (dotted).

non-optimal anti-reflection coating at larger angles. This along the non-uniform (Gaussian) shape of the gain curve of the Nd doped YAG host explains the rather large drop of power at the corners of the dotted curve in fig. 4.13. Figure 4.14 compares the result of the experiment with cold cavity output power. In this figure, the gain curve of the Nd:YAG crystal is assumed Lorentzian.

4.4 Conclusion

In this chapter, we explained the details of an experimental set-up, based on polarization multiplexing the gain arms, to study Michelson-type cavities. This designed set-up allows us to study the behavior of different cavity parameters, in particular, the output power and dominant eigenmode as a function of path-length error between the gain arms. The results from standard Michelson cavity, generalized Michelson cavity, and standard Michelson cavity with large path-length difference between the arms confirm that modal analysis of the previous chapter

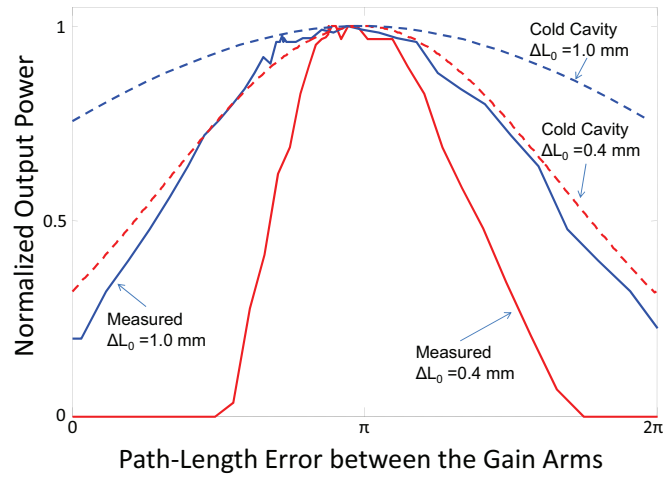


Figure 4.14: Output power for cavities with $\Delta L_0 = 0.4$ mm , $\Delta L_0 = 1.0$ mm. Solid lines are the experimental results and dashed lines are cold cavity analysis results.

accurately predicts the main characteristics of the Michelson-type cavities. The results also verify the role of spatial and longitudinal supermodes of the collective lasing system in abating the sensitivity of the output power to random path-length variation of the gain arms.

Chapter 5

Mode Shaping

The supermodes of most coherently combined cavities, including the self-Fourier and evanescently coupled cavities studied in chapter 2, contain many lobes. Since the power delivered to a single point is of primary interest in most applications, these supermodes, in their original forms, may not be suitable. The process of converting the supermode into a desired shape is called mode shaping.

Mode shaping can be performed by manipulating the amplitude (adding loss elements), and/or phase of the supermode's individual lobes. The amplitude techniques are simpler to implement, but due to their inherent lossy nature, they are not the method of choice, especially where higher power is intended. The phase techniques, though more difficult to implement, can be designed to have very high efficiencies.

This chapter is organized as follows. Section 5.1 reviews the definitions of some beam evaluation parameters, including Strehl ratio, overlap ratio, radiance, and M^2 . Section 5.2. divides the phase-based mode shaping techniques into two categories, superposition and aperture filling. Section 5.3. reviews a currently practiced aperture-filling technique and explains its efficiency limitations. Section 5.3. introduces a theoretically 100% efficient aperture-filling technique. Section 5.4. presents the design procedure and results of the experiment designed to verify this new technique. Section 5.5. compares the new technique with some of the

current techniques and reveals the underlying similarities and differences between them. Finally, section 5.6. concludes this chapter.

5.1 Beam Evaluation Parameters

It is clear that to evaluate the efficacy of beams for a particular application, a set of parameters is required. In some applications we are interested only in the behavior of the beam at one plane. In these cases, we compare the beams based on their strehl ratio or overlap coefficient. In some other applications, the propagating properties of the beam are more important. In these cases, beams can be compared based on parameters like radiance, or beam quality (M^2). Here we briefly define some of these parameters.

5.1.1 Strehl Ratio

Strehl ratio is defined as the ratio of the on-axis intensity at the far-field to the far-field on-axis intensity of the uniformly illuminated aperture. Since the uniformly illuminated aperture with amplitude k generates the on-axis far-field of $I_u(0,0) = (\frac{1}{\lambda_z})^2 k^2 A^2$, where A is the total area of the beam in the near-field, the Strehl ratio is given by

$$\text{Strehl Ratio} = \frac{I(0,0)}{I_u(0,0)} = 1/.$$

In a real source, the complex amplitude of the field in the near-field is not constant over emitting aperture, and therefore the Strehl ratio is reduced from unity by non-uniformities amplitude and phase distribution.

It can be shown that the Strehl ratio of any beam is approximately equal to the beam fill factor (the ratio of the area of the beam containing light and the total area of the mode), assuming the phase of the mode is uniform. This observation suggests that for the maximum Strehl ratio, the ideal near-field amplitude distribution should be uniform both in magnitude and phase.

In most beam combining applications of mode shaping, the goal is to concentrate more power in the central lobe. In this sense, increasing the fill-factor remains one of the main concerns of beam combining. In the rest of this chapter, when we discuss the beam combining techniques, unless otherwise stated, their potential to improve the Strehl ratio is evaluated.

5.1.2 Overlap Ratio

In applications other than beam combining, the actual shape of the beam might be of primary importance. In these cases, the overlap ratio defined as

$$\text{Overlap Ratio} = \frac{\int_{-\infty}^{+\infty} \int_{-\infty}^{+\infty} |U(f_x, f_y) U_d(f_x, f_y)|^2 df_x df_y}{\int_{-\infty}^{+\infty} \int_{-\infty}^{+\infty} |U(f_x, f_y)|^2 df_x df_y}$$

can be evaluated. The overlap ratio shows the correlation between the the far-field distribution $U(f_x, f_y)$ and the desired distribution $U_d(f_x, f_y)$.

5.1.3 Radiance and spectral radiance

Radiance and spectral radiance are radiometric measures that describe the amount of light that passes through or is emitted from a particular area, and falls within a given solid angle in a specified direction. The *SI* unit of radiance is watts per steradian per square meter ($W sr^{-1} m^{-2}$).

$$L = \frac{d^2\Phi}{dA d\Omega \cos\theta}$$

where the approximation only holds for small A and Ω where $\cos(\theta)$ is approximately constant. Here,

Φ is the total radiant flux or power (W) emitted,

θ is the angle between the surface normal and the specified direction,

A is the area of the source (m^2),

Ω is the solid angle (sr) subtended by the observation or measurement.

Radiance characterizes total emission or reflection, while spectral radiance characterizes the radiance at a single wavelength or frequency. The radiance is

equal to the sum (or integral) of all the spectral radiances from a surface. Spectral radiance has *SI* units ($Wsr^{-1}m^{-2}Hz^{-1}$ when measured per unit frequency interval, and ($Wsr^{-1}m^{-3}$) when measured per unit wavelength.

The radiance divided by the index of refraction squared is invariant in geometric optics. This means that for an ideal optical system in air, the radiance at the output is the same as the input radiance. This is sometimes called conservation of radiance. For real, passive, optical systems, the output radiance is at most equal to the input, unless the index of refraction changes.

5.1.4 Beam Quality factor (M^2)

The beam quality of a laser beam can be defined in different ways, but is essentially a measure of how tightly a laser beam can be focused under certain conditions (e.g. with a limited beam divergence). According to ISO Standard, it is defined as the beam parameter product (the product of a laser beam's divergence angle (half-angle) and the radius of the beam at its narrowest point (the beam waist)) divided by $\frac{\lambda}{\pi}$, the latter being the beam parameter product for a diffraction-limited Gaussian beam with the same wavelength. Determining the M^2 factor of the beams with more complex distributions like the supermodes of the self-Fourier and evanescently coupled cavities requires more considerations [27].

The M^2 factor of a laser beam limits the degree to which the beam can be focused for a given beam divergence angle, which is often limited by the numerical aperture of the focusing lens. Together with the optical power, the beam quality factor determines the radiance of a laser beam.

5.2 Review of Mode-Shaping Techniques

A supermode typically consists of several lobes, each lobe is generated by one of the gain elements. The geometric characteristics of the array determine the distance between the lobes and the size of each lobe. Depending on the coupling

mechanism utilized in the coherent beam combining architecture, the elements of the array may or may not equally contribute to the supermode, for example, the supermode of the self-Fourier cavity is consisted of Gaussian beams with a Gaussian envelope and the supermodes of the evanescently coupled cavities have sinusoidal envelopes.

The phase-based mode shaping for beam combining applications divides into two main categories: superposition and aperture-filling techniques. These techniques are shown in figs. 5.1 a and b. The superposition technique superimposes beams on top of each other. The aperture filling technique, on the other hand, creates a uniform near-field by filling the gaps between the array elements.

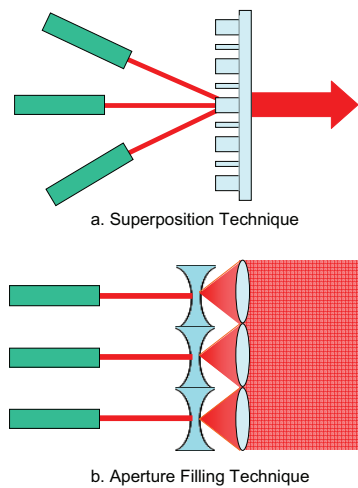


Figure 5.1: a) Superposition beam combining, and b) aperture filling techniques.

In fig. 5.1 a , the superposition technique uses a Dammann grating to superimpose the beams. Other phase components for beam superposition may include the beam splitter and volume holographic grating discussed in chapter 2. In comparison, the aperture filling technique in fig. 5.1 b uses an array of micro-lenses to fills the gap between the beams. It should be noted that the Dammann grating, beam-splitter, volume grating, and the array of micro-lenses can be designed to

be phase-only elements.

The superposition and aperture filling techniques both fail to work well for large arrays with low fill factors. The phase structure of the Dammann grating becomes considerably more difficult to fabricate, as the number of the gain elements increase. Similarly, in aperture filling technique, lenses with higher numerical aperture are required to enlarge the individual lobes to the optimum size, as the fill-factor of the array decreases.

The rest of this chapter studies aperture filling techniques that eliminate the need for the array of the micro-lenses.

5.3 Swanson Aperture Filling Technique

Swanson et. al.[29] proposed an aperture filling technique to convert amplitude non-uniformities to phase non-uniformities based on an enhanced inverse Zernike effect. Zernike's phase contrast microscope applies a 90 degree phase shift to the central region of the far field (or spatial Fourier transform domain) to convert small phase variations to amplitude variations[30]. Swanson's beam combining technique utilizes Zernike's method in the reverse direction to convert non-uniformities in amplitude into non-uniformities in phase. A phase plate is then employed to cancel the resulting phase non-uniformities. This method has been called aperture filling by amplitude-to-phase conversion. Figure 5.2 illustrates the Swanson's aperture filling technique. Swanson also proved that for optimal amplitude-to-phase conversion the necessary phase shift in the Fourier plane must be $\Phi = \arccos\left(\frac{2F}{2F-1}\right)$, where F is the array fill factor.

An example is given in fig. 5.3 to understand the Swanson technique. Assume that the mode is a periodic distribution of square beams with fill-factor (F) of 0.25. The DC term (zero-order in the Fourier domain) is equal to the average of this distribution (0.25). For 0.25 fill-factor, Swanson suggests to add a π phase shift to the central order in the Fourier domain. The π phase shift in the zero-order subtracts 0.5 from the whole array in the new near-field (corrector plane).

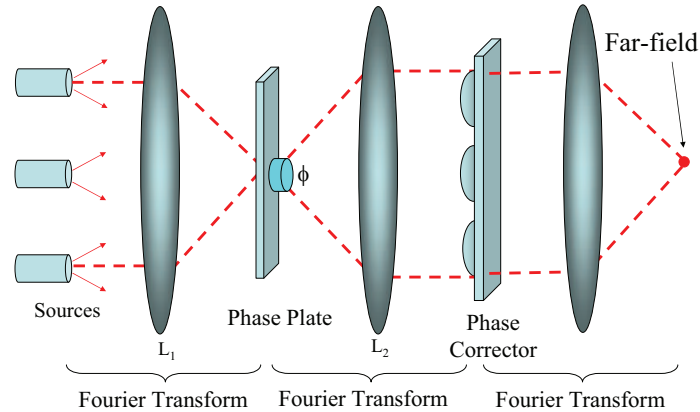


Figure 5.2: Swanson's amplitude to phase conversion technique.

The near-field before the corrector plate, as a result, will be uniform in amplitude and nonuniform in phase. The corrector plate then compensates the phase non-uniformities to generate a distribution uniform in both amplitude and phase. The far-field (Fourier-transform) of this uniform distribution concentrates all the power into the central order.

The two requirements for Swanson's amplitude-to-phase conversion method to work with 100% efficiency are 1) the array modes must consist of binary amplitudes, and 2) the two-dimensional fill factor must be greater than 25%. Deviation from these ideal conditions directs some of the power to the higher order lobes. These two requirements limit the applicability of the Swanson method. For reduced fill factors or non-binary amplitude profiles, the efficiency can drop quickly to considerably lower values.

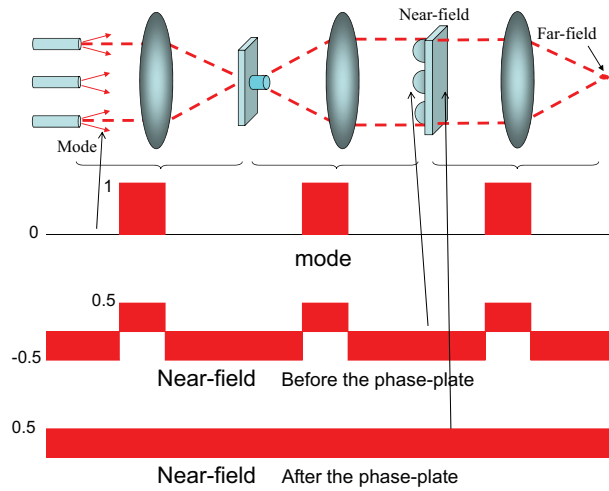


Figure 5.3: An example of a Swanson's amplitude to phase conversion technique.

5.4 Generalized Amplitude-to-Phase Conversion

We identified that the source of the limitations of Swanson method lies in the restriction to modify only the central lobe of the Fourier plane (as in Zernike's microscope). Viewed from a different perspective, this optical system can be cast in terms of a phase retrieval problem. The phase retrieval problem, as shown schematically in fig. 5.4, finds the phases in two conjugate planes such that a set of amplitude constraints is satisfied [32].

In mode shaping, this viewpoint allows for changing the phase of multiple orders in the Fourier plane with the goal of producing an all-phase function in the output plane. In this section we show that modifying these higher-order Fourier components resolves both limitations of Swanson's method and offers virtually a 100% combining efficiency for any individual laser beam profile and for any fill factor. We call this new method, the generalized amplitude-to-phase conversion, to differentiate it from Swanson's method.

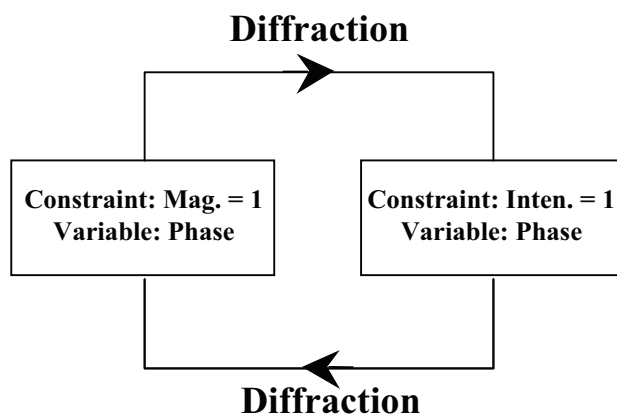


Figure 5.4: A diagram representation of the Gerchberg-Saxton algorithm.

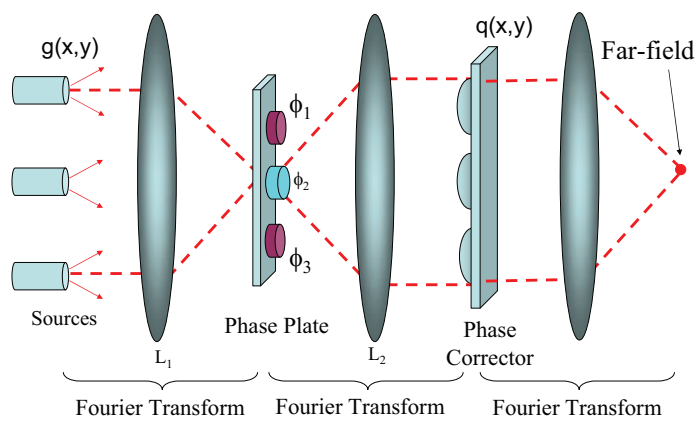


Figure 5.5: Generalized amplitude to phase conversion technique.

Figure 5.5 shows the generalized amplitude-to-phase conversion beam combining scheme. The complex amplitude of the laser array mode profile is given by $g(x, y)$, where this field is assumed to be quasi-periodic. The corresponding complex field in the back focal plane of lens L1 is given by the Fourier transform of $g(x, y)$. Note that this field occurs in discrete points or diffraction orders, due to the assumed periodicity in the source. The resultant field $S(f_x, f_y)$ after passing through the phase plate $P_1(f_x, f_y)$ is given by $S(f_x, f_y) = F\{g(x, y)\} \times P_1(f_x, f_y)$, where F indicates a two-dimensional spatial Fourier transformation. Finally, the field at the corrector plane $q(x, y)$ is given by $q(x, y) = F\{S(f_x, f_y)\} \times P_2(x, y)$, where $P_2(x, y)$ is a phase-only function representing the phase corrector. The geometry of the system requires $|S(f_x, f_y)| = |F\{g(x, y)\}|$, and the criterion for 100% efficient beam combining requires $q(x, y) = 1$. Given these two criteria in the Fourier and the corrector planes, a phase retrieval algorithm [35] which is a modification of the GerchbergSaxton algorithm iterative method of fig. 5.4 finds the optimal profiles of the phase plates.

Table 5.1 confirms the superiority of this approach to Swanson's amplitude-to-phase conversion technique for arrays with low fill-factor and for deviations from square beams.

Table 5.1: Comparison between single-order (Swanson's) method and multi-order (generalized) method.

Shape	Square	Gaussian	Square
Fill factor	25%	25%	10%
Efficiency (single-order)	100%	89%	70%
Efficiency (multi-order)	100%	99.9%	99.9%

5.5 Experimental Results

An experiment was performed to combine light from a self-Fourier mode [36] with a fill-factor of 13.9%. We generated our self-Fourier mode by illuminating an appropriately designed half-tone mask shown in fig. 5.6, with an expanded, collimated laser beam to guarantee perfect mutual coherence between the individual Gaussians in the mode. Spatial filtering was applied to reconstruct the desired mode from the mask. The phase shifts in the Fourier domain and the phase corrector plate in the output plane were implemented by computer generated holograms. Of course, in an actual system, special phase shifters and phase plates with negligible loss would be used. However, the holographic technique offers a flexible method to experiment with a variety of configurations.

The holographic implementation of the discrete phase shifters in the Fourier plane consisted of simple binary gratings at each diffraction order, where spatial shifts between individual gratings encode the appropriate phase. The continuous phase plate in the output plane is fabricated using Lohmann's computer hologram coding technique [33]. The second and third holograms are designed to generate the appropriate distribution in the 1st and -1st orders, respectively. The half-tone (first structure) generates the desired pattern in the zero order.

Figure 5.7 shows the results of the experiment. The right side of fig. 5.7 shows the measured far-field intensity when no beam combining optics is applied (Fourier plane). Since the mode was chosen to be self-Fourier, this far-field pattern is seen to resemble the near-field pattern very closely. The left side of fig. 5.7 shows the far-field pattern when the beam combining optics of this paper are applied.

Figure 5.8 compares the theoretical expectations with the experimental results. With perfect compensation of the phases this beam combining technique should have directed 97% of the energy into the central spot. Experimentally we measured 72% of the energy in the central lobe. Though smaller than 97% expected from the theory, this result means the measured power in the central lobe is increased by a factor of 5 (72%/13.9%).

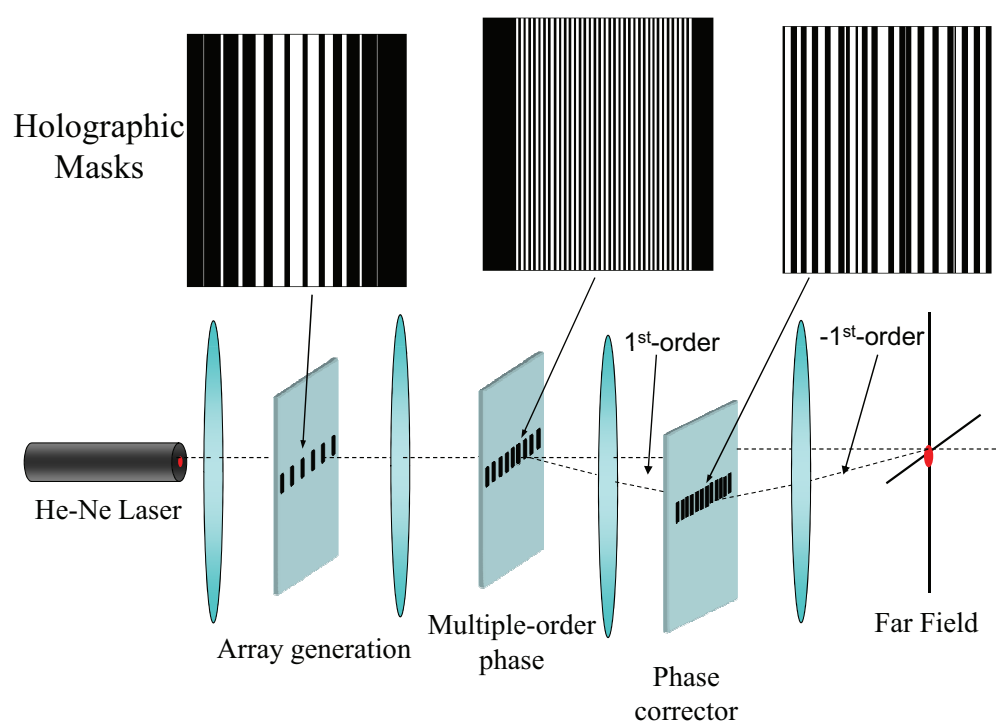


Figure 5.6: Experimental set-up for generalized amplitude-to-phase conversion technique.

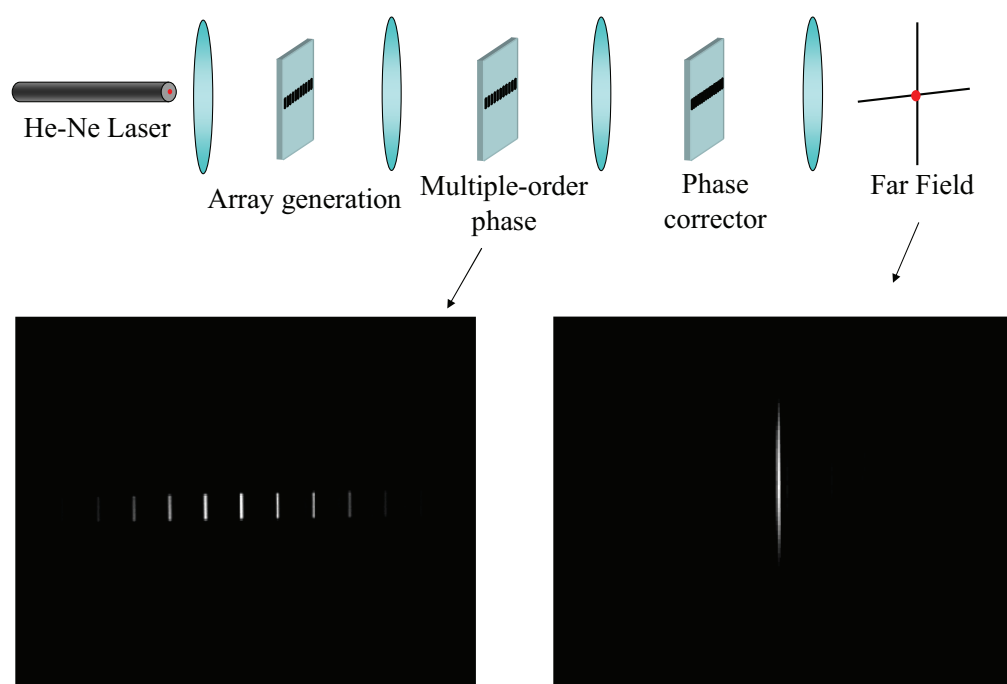


Figure 5.7: Experimental results of the generalized amplitude to phase conversion technique.

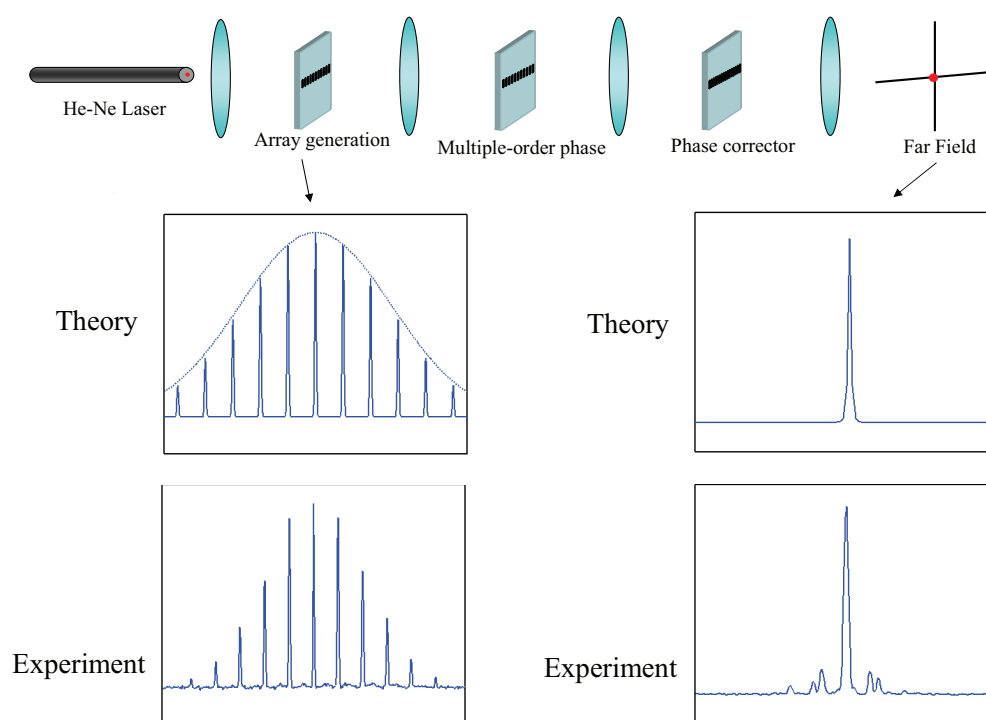


Figure 5.8: Comparison between the theoretical predictions and experimental results of the generalized amplitude to phase conversion technique .

First of all, in the design of the first hologram (half-tone), it is assumed that the expanded He-Ne laser beam is uniform. However, since our array was considerably large (11 elements), the intensity of the expanded beam decreases away from the center. As a result the generated array is not a perfect self-Fourier. Second, the aberrations of the second and third Fourier lenses that are used in an angle changes the result. Finally, the pattern of the phase corrector is more complex.

5.6 Comparison: Dammann Grating and Aperture Filling Techniques

It is possible to make a connection between aperture filling by Swanson's amplitude-to-phase conversion method, the current technique of generalized amplitude-to-phase conversion utilizing multiple orders, and the Dammann grating technique for beam superposition [34]. Clearly, the current generalized amplitude-to-phase conversion is most similar to Swanson's single-order amplitude-to-phase conversion method, where higher-order grating lobes are employed to increase efficiency and remove the fill-factor and mode profile constraints. The relationship to the Dammann grating technique is slightly more subtle. In fig. 5.9, the current technique is compared to the Dammann superposition technique. Both techniques involve modifying the phase in two planes. Similar to the generalized amplitude-to-phase conversion method, the Dammann grating design consists of two steps; the first step selects appropriate phases for the individual beams from the coherent array to ensure a quasi-uniform magnitude in the back focal plane of the lens. The second step corrects the resulting phase non-uniformities. Since the coherent laser beam array has an essentially discrete angular plane wave spectrum, the corrector plate is periodic and takes the form of a phase grating (Dammann grating). We see that this design procedure can also be cast as a phase retrieval problem, where the optimal choice of the phases in the two planes is governed by the above magnitude constraints.

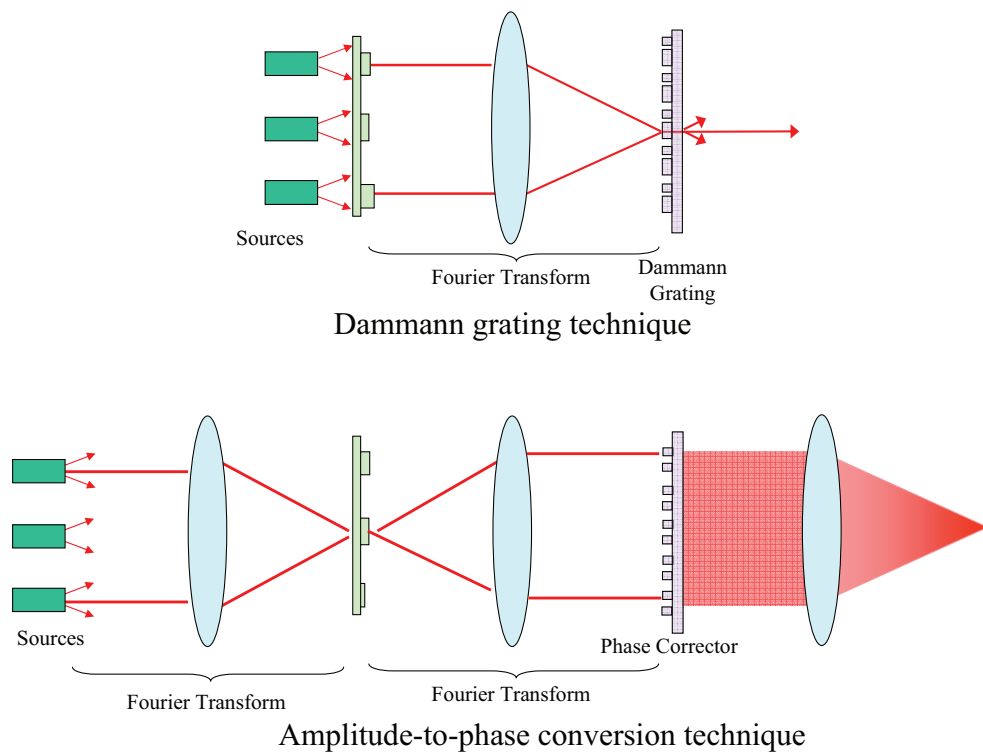


Figure 5.9: Comparison between the superposition technique with Dammann grating and the generalized amplitude-to-phase technique.

A comparison between our generalized amplitude-to-phase conversion method and the Dammann grating beam combining method reveals the underlying connection between the aperture-filling and the superposition techniques. Clearly, they both manipulate the phase of the array mode in two conjugate (Fourier) planes to affect the mode conversion (although in many practical coherent laser beam combining cases the Dammann grating method uses the intrinsic phases of the laser array as a substitute for the first phase plate [37]). More generally, it is clear from fig. 5.9 that the principle difference between the two methods is that the Dammann grating applies the first phase modification to the near-field of the laser distribution, and the second phase plate to the far-field (Fourier transform), whereas the generalized amplitude-to-phase conversion method proposed in section 5.4 applies the first phase modification to the far-field pattern produced in the Fourier transform plane of the first lens, and the second phase plate to the near field distribution (or its image formed at the back focal plane of the second lens).

The Fourier relationship between the amplitude-to-phase conversion technique and the Dammann grating superposition method immediately suggests that the strength of one is likely to be the weakness of the other. For example, we note that aperture filling by generalized amplitude-to-phase conversion is not sensitive to an increase in the number of lasers in the array. Indeed, in theory the technique works for an infinite array of lasers. However, using the Dammann grating technique with a larger number of lasers requires a more complex grating design and can lead to a grating that is physically difficult to fabricate. This is shown in fig. 5.10, where the increased complexity of the Dammann grating for 51 lasers in fig. 5.10(b) is immediately evident compared with one designed for 3 lasers in fig. 5.10(a).

Conversely, reducing the mode fill factor when applying aperture filling by generalized amplitude-to-phase conversion increases the complexity of the second phase plate, whereas the Dammann grating is essentially insensitive to fill factor and can accommodate virtually any fill factor requirement by simply adjusting the

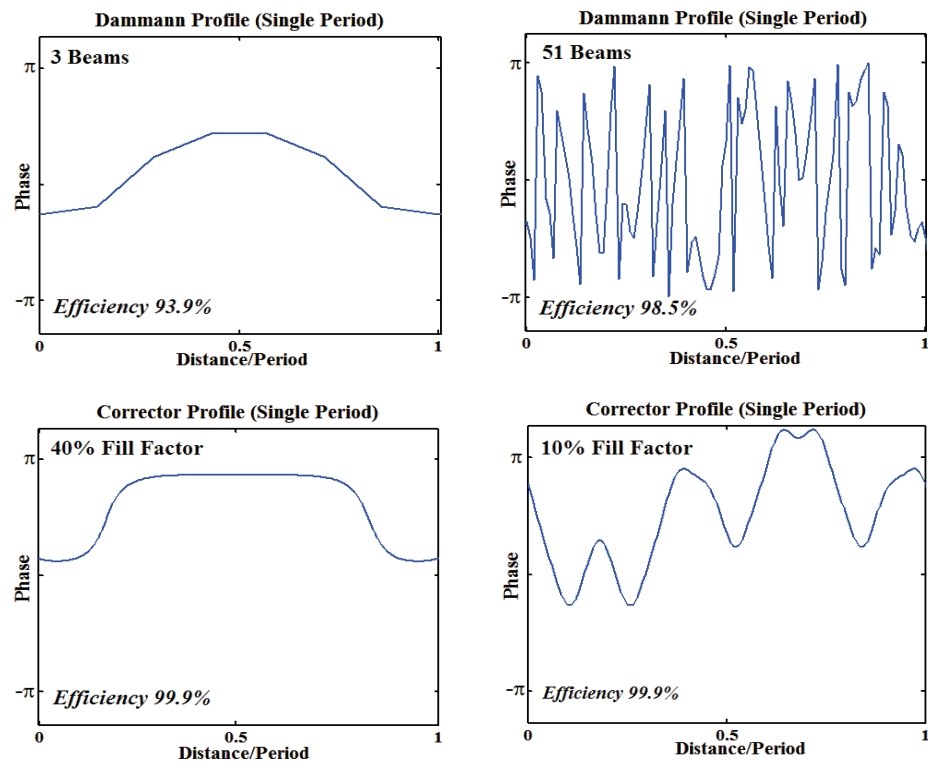


Figure 5.10: Comparison between the phase plates in superposition technique with Dammann grating and the generalized amplitude-to-phase technique.

pitch of the grating. The fill factor sensitivity of the generalized amplitude-to-phase aperture filling technique is shown in fig. 5.10(c) and 5.10(d) by comparing a single period of the aperture filling corrector plate for a 40% fill factor (fig. 5.10(c)) and a 10% fill factor (fig. 5.10(d)). Note also that aperture filling by generalized amplitude-to-phase conversion has a theoretical combining efficiency that is slightly higher than the Dammann grating.

Finally, in high-power beam combining, it is undesirable to concentrate power in any of the intermediate planes. As described in this chapter, both the Dammann grating and generalized aperture filling require focusing (fig. 5.9). In such cases, the focal length of the lens ultimately determines the concentration of power. In the Dammann grating beam combining technique, however, the beams can be deflected by nonfocusing means [28]. Since the intensity at the grating plane increases owing to the superposition of beams, the concentration of power can be lowered to the desired level by adequately expanding the individual beams before reaching the grating ($\frac{Power}{Area} = \frac{NP}{d^2}$). In comparison, the aperture-filling technique requires a proper balance among the size of the beams, the number of array elements, and the focal length of the Fourier lens to prevent unwanted power concentration in the Fourier plane $\frac{Power}{Area} = \frac{NP}{d^2} \left(\frac{Nd^2}{\lambda f}\right)^2$, where $power = NPF^2$, $F = \left(\frac{d}{D}\right)^2$ and $Area = \left(\frac{\lambda f}{ND}\right)^2$. This means to have the same power concentration as the Dammann grating technique, the aperture filling technique requires a lens with a focal length of $f = \frac{Nd^2}{\lambda}$.

5.7 Conclusion

In summary, we have introduced a new beam combining technique that is theoretically capable of 100% combining efficiency under a wide variety of beam shapes and fill factors, and have demonstrated the technique experimentally with a self-Fourier mode. We have shown that our new method is related both to Swanson's amplitude-to-phase conversion method and the Dammann grating beam combining method. In particular, it forms a Fourier conjugate relationship with the

Dammann grating technique, making it the method of choice for large numbers of lasers. The significance of this work is that it provides a guideline to perform beam shaping in discrete and continuous sense on any beam with theoretically 100% efficiency.

Chapter 6

Conclusion and Discussion

The modal analysis was utilized to explain and compare the coherent beam combining characteristics of several laser common cavities. The modal analysis showed that while many of these cavities can establish coherence between the gain elements, the path-length error caused by environmental changes or inherent nonlinear properties of the gain elements ultimately reduces the output power generated by these cavity to the power generated by a single gain element. To reduce this sensitivity to random path-length variations of the gain elements, it has been suggested to properly exploit the spatial and longitudinal modes of the common cavity. The sensitivity reduction by utilizing spatial modes suggests that additional reflectors in Michelson architecture brings a significant amount of otherwise lost power to the cavity. The cavity with large path-length difference between the gain arms also shows high sensitivity to random path-length variations.

To compare the benefits of these two technique we define the combining efficiency (*C.E.*) as

$$C.E. = \frac{\dot{P}_o}{N\dot{P}_g} \quad (6.1)$$

where \dot{P} refer to circulating power inside the cavity, and N is the number of gain elements. Using this formula, it is easy to see that for the Michelson cavity, in the spatial-mode-dominated regime the maximum attainable C.E. is 81%, and in

the longitudinal-mode-dominated regime the C.E. can indefinitely approaches to 100%.

It is natural to ask whether the benefits of the recycling mirror geometry (spatial modes) or the large length mismatch (longitudinal modes) can be extended to combine larger numbers of lasers. For spatial modes, simulations of straightforward extensions of the technique indicate that there is always a benefit to using this architecture, but that the magnitude of this benefit is reduced as the number of lasers increases. The simulations suggest that the efficiency drop follows the empirical formula given by

$$C.E. = (0.81)^{\log_2 N} \quad (6.2)$$

where N is the number of gain elements. The efficiency of the longitudinal mode technique also drops with increasing the number of gain elements. Obviously, For larger number of gain elements, finding a common longitudinal mode becomes more difficult. Figure ?? shows the Monte Carlo simulation of the combining efficiency of the longitudinal mode technique as a function of the number of gain elements.

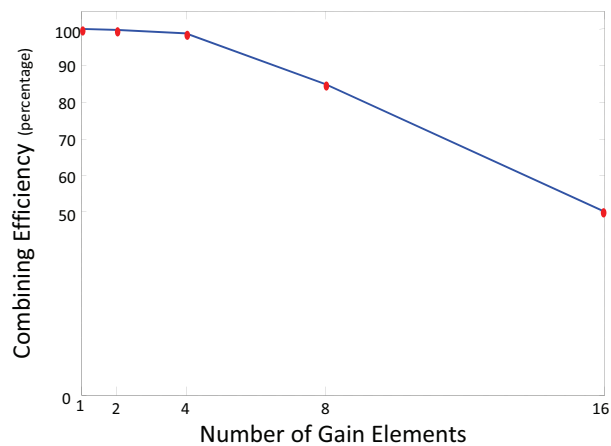


Figure 6.1: Combining efficiency as a function of the number of gain elements, in a cavity that longitudinal mode techniques is applied.

The spatial and longitudinal techniques can be exploited simultaneously to achieve the best results. Figure 6.2 shows the combining efficiency in cavities where both longitudinal and spatial mode techniques are applied.

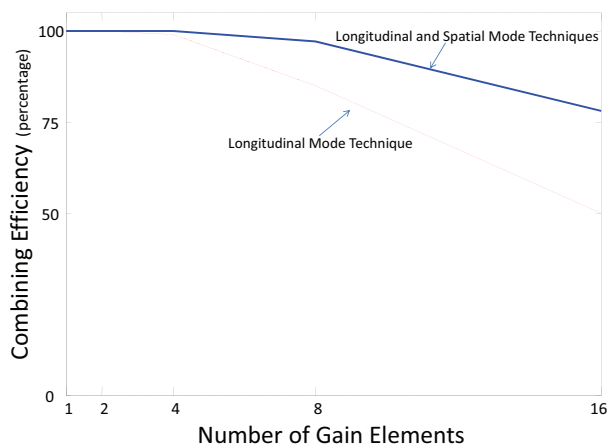


Figure 6.2: Combining efficiency as a function of the number of gain elements, in a cavity that both longitudinal and spatial mode techniques are applied.

Finally, it should be noted that we have only considered one class of coherent combining architectures in this paper; namely, laser beam superposition (Michelson, Dammann grating, volume Bragg grating) cavities. Other classes of combining architectures such as spatial filtering, Talbot, and Self-Fourier cavities may also benefit from modifying the resonator filtering function to trade modal discrimination for some degree of phase tolerance.

References

- [1] T. Y. Fan, “*Laser beam combining for high-power, high-radiance sources*”, IEEE J. Sel. Top. Quantum Electron. 11, 567-577 (2005).
- [2] J. R. Leger, “*External methods of phase locking and coherent beam addition of diode lasers, in Surface Emitting Semiconductor Lasers and Arrays*”, G.A.Evans and J.M.Hammer, eds. (Academic, 1993), pp. 379-433.
- [3] E. Kapon, J. Katz, and A. Yariv, “*Supermode analysis of phase-locked arrays of semiconductor lasers*”, Opt. Lett. 9, 125-127 (1984)
- [4] Marshall, W.; Katz, J., “*Direct analysis of gain-guided phase-locked semiconductor laser arrays*”, Quantum Electronics, IEEE Journal of , vol.22, no.6, pp. 827-832, (1986)
- [5] D. Botez, L. J. Mawst, G. Peterson, and T. J. Roth, “*Resonant optical transmission and coupling in phase-locked diode-laser arrays of antiguides: The resonant-optical-waveguide array*”, Appl. Phys. Lett., vol. 54, pp. 2183-2185, May 1989
- [6] Philipp-Rutz, E., “*Spatially coherent beam formation and mode locking of an array of solid-state lasers*”, Quantum Electronics, IEEE Journal of , vol.14, no.2, pp. 112-118, Feb 1978
- [7] R. H. Rediker, R. P. Schloss, and L. J. Van Ruyven, “*Operation of Individual Diode Lasers as a Coherent Ensemble Controlled by a Spatial Filter within an External Cavity*”, Appl. Phys. Lett. 46, 133 (1985).

- [8] A. A. Golubentsev, V. V. Likhanskii, and A. P. Napartovich, "*Theory of Phase Locking of an Array of Lasers*," Sov. Phys. JETP 66, 676682 (1987).
- [9] Leger, James R. "*Lateral Mode Control of an AlGaAs Laser Array in a Talbot Cavity*", Appl. Phys. Lett. 55, 334-336 (1989).
- [10] J. R. Leger, G. J. Swanson, and W. B. Veldkamp, "*Coherent laser addition using binary phase gratings*", Appl. Opt. 26, 4391-4399 (1987)
- [11] C.J. Corcoran and F. Durville, "*Experimental demonstration of a phase-locked laser array using a self-Fourier cavity*", Applied Physics Letters 86, 201118-1-3 (2005)
- [12] J.R. Andrews, "*Traveling-wave amplifier made from a laser diode array*", Appl. Phys. Lett. 48, 1331-1333 (1986)
- [13] Eric C. Cheung, James G. Ho, Gregory D. Goodno, Robert R. Rice, Josh Rothenberg, Peter Thielen, Mark Weber, and Michael Wickham, "*Diffraction-based beam combination of a phase-locked fiber laser array*", Optics Letters 33, 354-356 (2008).
- [14] M. Segev, S. Weiss and B. Fischer, "*Coupling of Diode Laser Arrays with Passive Phase Conjugate Mirrors*", Appl. Phys. Lett. 50, 1397, (1987)
- [15] J.K. Butler, D.E. Ackley, and D. Botez, "*Coupled-mode analysis of phase-locked injection arrays*", Applied Physics Letters 44, 293-295 (1984)
- [16] D. Mehuys, W. Streifer, R. G. Waarts, and D. F. Welch, "*Modal analysis of linear Talbot-cavity semiconductor lasers*", Opt. Lett. 16, 823-825 (1991)
- [17] C. J. Corcoran, K. Pasch, "*Modal analysis of a self-Fourier laser cavity*", J. Opt. A: Pure Appl. Opt. 7 L1-L7 (2005).
- [18] J. R. Leger, "*Laser Beam Shaping*," Microoptics, H. P. Herzig, ed., Taylor and Francis, London (1996).

- [19] A. Shirakawa, T. Saitou, T. Sekiguchi, and K. Ueda, “*Coherent addition of fiber lasers by use of a fiber coupler*”, Opt. Express 10, 1167-1172 (2002)
- [20] A. G. Fox, T. Li “*Resonant modes in a maser interferometer*”, Bell Syst. Tech. J. 40:453-88, 1961.
- [21] H. Dammann, “*Blazed synthetic phase-only holograms, Optik 31 (1970)*”, pp. 95 104
- [22] J. R. Leger, G.J. Swanson, and W. B. Veldkamp, “*Coherent laser addition using binary phase gratings*”, Appl. Optics 26, 4391-4399 (1987).
- [23] J. R. Fienup, “*Phase retrieval algorithms: a comparison,*” Appl. Opt. 21, 2758-2769 (1982)
- [24] M. Khajavikhan, A. Hoyer-Leitzel, J. R. Leger “*Efficient conversion of light from sparse laser arrays into single-lobed far-field using phase structures*”, Opt. Lett. 33, 2377-2379 (2008).
- [25] P. Laures, “*Variation of the 6328 A Gas Laser Output Power with Mirror Transmission*”, Physics Letters, 10, pp. 61-62, 15 May 1964
- [26] Kouznetsov, D.; Bisson, J.; Shirakawa, A.; Ueda, K., “*Limits of coherent addition of lasers: simple estimate,*” Lasers and Electro-Optics, 2005. CLEO/Pacific Rim 2005. Pacific Rim Conference on , vol., no., pp. 1061-1063, 30-02 Aug. 2005
- [27] A. E. Siegman, ”How to (Maybe) Measure Laser Beam Quality, “Tutorial presentation at the Optical Society of America Annual Meeting, Long Beach, California, October 1997
- [28] J. R. Leger, ”External Methods of Phase Locking and Coherent Beam Addition,” Chapter 8 of the book Surface Emitting Diode Lasers and Arrays, G. Evans and J. Hammer, ed., Academic Press, New York (1993) (55 pages)

- [29] G. J. Swanson, J. R. Leger, and M. Holz, "Aperture filling of phase-locked laser arrays," *Opt. Lett.* 12, 245- (1987)
- [30] F. Zernike, "How I discovered phase contrast," *Science* 121, 345-349 (1955)
- [31] J. Glckstad, "Phase contrast image synthesis," *Opt. Commun.* 130, 225-230 (1996)
- [32] R. W. Gershberg and W. O. Saxton, *Optik* 35, 237-246 (1972)
- [33] B. R. Brown and A. W. Lohmann. Computer-generated binary holograms. *IBM J. Res. Develop.*, 160-168, (1968).
- [34] J.R. Leger, G.J. Swanson, and W. B. Veldkamp, "Coherent laser addition using binary phase gratings," *Appl. Optics* 26, 4391-4399 (1987).
- [35] J. R. Fienup, "Phase retrieval algorithms: a comparison," *Appl. Opt.* 21, 2758-2769 (1982)
- [36] C. Corcoran and K. Pasch, "Modal analysis of a self-Fourier laser cavity," *J. Opt. A, Pure Appl. Opt.* 7, L1-L7 (2005)
- [37] E. C. Cheung, J. G. Ho, G. D. Goodno, R. R. Rice, J. Rothenberg, P. Thielen, M. Weber, and M. Wickham, "Diffractive-optics-based beam combination of a phase-locked fiber laser array," *Opt. Lett.* 33, 354-356 (2008)